AN INTEGRATED GEOPHYSICAL AND GEOCHEMICAL APPROACH TO CHARACTERIZING ACID MINE DRAINAGE IN A HEADWATER MOUNTAIN STREAM IN COLORADO, USA

by

Allison Johnston

A thesis submitted to the Faculty and the Board of Trustees of the Colorado School of Mines in partial fulfillment of the requirements for the degree of Master of Science (Hydrology).

Golden, Colorado

Date ______________________________

Signed: __________________________________
Allison Johnston

Signed: __________________________________
Dr. Kamini Singha

Golden, Colorado

Date ______________________________

Signed: __________________________________
Dr. Terri Hogue
Professor and Program Director
Hydrologic Science and Engineering

ABSTRACT

This study integrates geochemical sampling, fluid electrical conductivity (σ_f) logging, electromagnetic induction (EMI), and electrical resistivity imaging (ERI) to investigate the impact of acid mine drainage (AMD) from the Minnesota Mine, an inactive gold and silver mine, on Lion Creek, a headwater mountain stream near Empire, Colorado. The study goal is to assist in evaluating remediation options by characterizing seasonal variation in AMD contamination levels and identifying the controls of point and diffuse sources of AMD entering Lion Creek. The pH and log (σ_f) of the water in Lion Creek inversely correlate, indicating that the low pH characteristic of AMD-impacted water correlates to high σ_f values that can serve as a target for the geophysical methods. ERI surveys were run along the east bank of Lion Creek along a reach where acidic water seeps out of the steep stream bank and into the creek. These ERI surveys identified two areas where diffuse contamination is likely entering the stream: (1) the subsurface extent of two seepage faces visible on the surface and (2) runoff leaching through a tailings pile on the east bank of Lion Creek. σ_f in the stream was lowest when the stream level was highest in the early summer and then increased throughout the summer as the stream level decreased, indicating that the concentration of dissolved solids in the stream is largely controlled by dilution due to snowmelt. Total dissolved solids (TDS) were calculated using an empirical relationship between σ_f and TDS, and TDS load (TDS concentration times stream discharge) was calculated. TDS load is greatest in the early summer and displays a large diel signal. This work will be helpful in informing remediation efforts because the identification of diffuse sources of AMD allows for more targeted remediation options and knowledge of seasonal variation is necessary in predicting the costs and outcome of different remediation scenarios.

TABLE OF CONTENTS

LIST OF FIGURES

LIST OF TABLES

ACKNOWLEDGEMENTS

Many people provided invaluable support for me throughout this research project. I would like to acknowledge my advisor, Kamini Singha for her guidance throughout the project. Our weekly meeting was extremely helpful in guiding my efforts and pushing me to a deeper understanding of my data set. My committee members, Andrei Swidinski, Alexis Navarre-Sitchler, and Rob Runkel provided valuable insight and suggestions. Dr. Alexis Navarre-Sitchler provided some key assistance with regards to the geochemical sampling methods and analysis, and Dr. Rob Runkel's experience in mine site investigation and its literature has proved invaluable. My fellow students have provided essential support, including assistance with field work, discussions of research ideas, and providing feedback on thesis drafts and presentations. In particular, thank you to Heewon Jung, Emily Voytek, Zack Walter, Sydney Wilson, Dave Rey and Aaron Bandler for their willingness to discuss ideas and review drafts and presentations. A heartfelt thank you to my field work helpers, Avery Becker, Zack Walter and Curtis Weller. Finally, thank you to Jackie Randall for lending her expertise for each of the methods employed in this study. Without her knowledge and assistance, this project could not have happened!

CHAPTER 1

GENERAL INTRODUCTION

There are thousands of inactive mines in the Colorado Mineral Belt, a legacy of the gold and silver rushes in the state's history (Lovering and Goddard 1950). Many of the mines have not been active for nearly a century, are poorly documented, and no longer have a clear owner or responsible party. These mines pose an environmental threat as water drains through mine adits and tailings piles, weathering the partially mined ore (e.g., Banks et al. 1997). Metal sulfides commonly contained in valuable ore release large amounts of proton acidity as they weather, a process known as acid rock drainage (e.g., Nordstrom 2011). This process occurs naturally across Colorado, but it is greatly accelerated by mining, which increases the surface area of ore exposed to weathering. The accelerated acid rock drainage is known as acid mine drainage (AMD) (e.g., Evangelou and Zhang 1995).

Pyrite, the most common metal sulfide, releases large amounts of proton acidity as it weathers (Evangelou and Zhang 1995; Chandra and Gerson 2010). Metal solubility increases in acidic water, which has the adverse effect of mobilizing other metals contained in the ore into the environment. Iron, aluminum, manganese and copper are often found dissolved in AMD water, but the exact chemistry depends on the minerology of the ore deposit (e.g., Nordstrom 2011). The combination of low pH and high metal concentrations is detrimental to aquatic life, and in some scenarios, hazardous to human health (DeNicola and Stapleton 2002; Niyogi et al. 2002).

Remediation of these sites if often difficult due to the lack of information from the period when the mine was active and lack of funds in the case of mines without a clear responsible party (e.g., Kimball et al. 2006). These challenges make site investigation a particularly important step in the remediation process, both to compensate for the lack of preexisting information and to determine the most cost effective scenario. Two challenges common to many inactive mine site investigations are identifying diffuse contamination sources and characterizing seasonal variation in AMD impact levels (August et al. 2002; Kimball et al. 2010; Gozzard et al. 2011).

This study takes place in the Empire Mining District, located approximately 100 km west of Denver, CO. The area has a history of gold and silver mining dating back to the late 1800s (Braddock 1969). Here, we explore the impacts of Minnesota Mine on Lion Creek, a small headwater mountain stream. Lion Creek's hydrograph is dominated by the pulse of spring runoff due to snowmelt at higher elevations. The site was the subject of a remediation effort in 1996 that focused on tailings removal and erosion control since the most serious concern at the time was the large amounts of sediment that were washed down through the town of Empire, CO during rainstorms (Dodson 2004). However, due to persistent water quality issues in Lion Creek, which is a tributary of Clear Creek, the United States Forest Service (USFS) is planning another remediation effort. The United States Geological Survey (USGS) has been involved in site characterization using a hydrologic tracer test and synoptic sampling to compile detailed information about metal loading to the stream.

This project aims to supplement the work done by the USGS using an integrated geophysical and geochemical approach to site characterization. The first step in this study was to make preliminary field observations in August 2014. We chose a 480 m reach of the stream for further study that encompasses an upstream section of the stream that appears to be unaffected by the mine to a downstream reach that is clearly mine impacted based on iron-oxide precipitates on the streambed, low pH water, and tailings deposited on the streambed. The study reach includes multiple seepage faces along the east bank of Lion Creek, where acidic water seeps out of the steep stream bank and mixes with stream water. Figure 1.1 gives an overview of the study reach and shows the spatial distribution of the three main surface seeps. The three seeps shown in the diagram are considered discrete sources of AMD since they are easily identifiable.

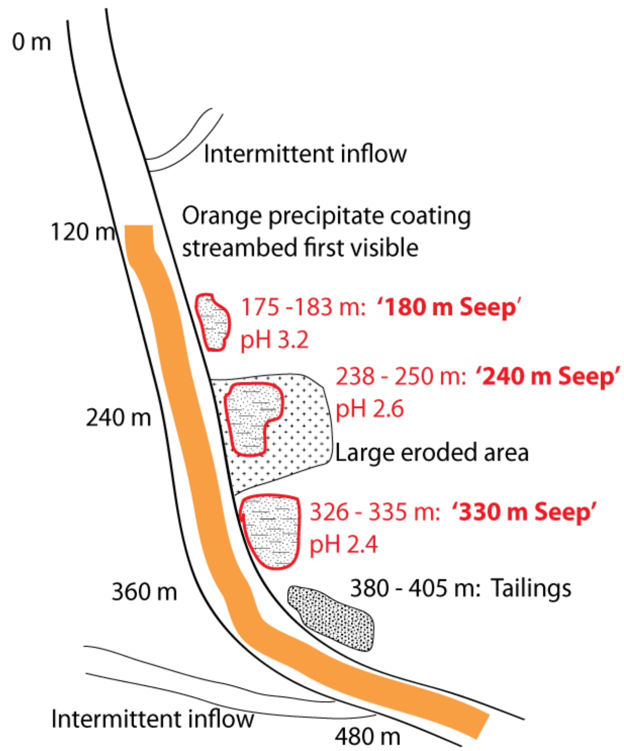

Figure 1.1: Diagram of Lion Creek study reach.

Figure 1.2 shows the 330-m seep, which has the lowest average pH of any of the main seeps at 2.4 standard pH units. The photo was taken facing downstream and to the south; the seepage face visible on the left side of the stream is on the east stream bank. The mine is located to the northeast of the seepage face pictured. As the low pH water from the seep mixes with higher pH stream water, metals contained in the seepage water become less soluble and precipitate out of the solution. This causes the orange coating seen on the streambed.

Figure 1.2: Photograph of the 330-m seep, taken in August 2014. The camera is facing downstream and to the south.

Though we were able to identify three discrete sources of AMD entering the stream in the form of seepage faces, the presence of orange iron precipitate on the streambed upstream of the seepage faces indicates that there are additional, likely diffuse, AMD pathways. Also, the fact that Lion Creek's hydrograph is snowmelt dominated means that there should be seasonal variation in the site hydrology, and therefore likely variation in contaminant levels and loads. The presence of diffuse sources as well as seasonal changes in hydrology indicates that a robust site characterization is necessary.

For this study, geochemical samples and a range of geophysical methods were employed. The selected geophysical methods are electrical resistivity imaging (ERI), electromagnetic induction (EMI) and fluid conductivity logging. ERI resolves changes in bulk electrical conductivity (σ_b) with depth, EMI allows us to quickly measure depth averaged σ_b of the shallow subsurface and fluid conductivity logging yields a time series of fluid electrical conductivity (σ_f) measurements. Geochemical samples were used to measure the concentrations of individual constituents, directly relating the σ_f measurements to the AMD constituents. The bulk of this study was conducted from May to October 2015, encompassing the snowmelt period to the late-summer drying-out period.

The geophysical methods were chosen because they measure σ_f or σ_b, which is sensitive to σ_f. AMD water has a high σ_f due to its high concentration of dissolved solids. Thus, the AMD water serves as an electrical tracer of sorts, and the σ_b and σ_f data can be used to determine the relative level of AMD water contribution. This is illustrated in Figure 1.3, which shows point measurements of pH and σ_f that were taken throughout the field season in Lion Creek and in the acidic seeps. The pH was plotted against the log10(σ_f) at each measurement location. This relationship has been leveraged in many AMD site investigation studies. One of the first of these studies was done by Merkel (1972), in which ERI was used to delineate the extent of AMD contamination in an aquifer. Another such study was done by Benson and Addams (1998) in which they used ERI to map the presence and level of contamination, which they correlated to drill logs and water samples at two different inactive mine sites in Utah. Ladwig (1983) discusses three case studies in which EMI was used to delineate the extent of AMD contaminated groundwater. There are numerous other applications of ERI and EMI to AMD site characterization described in literature.

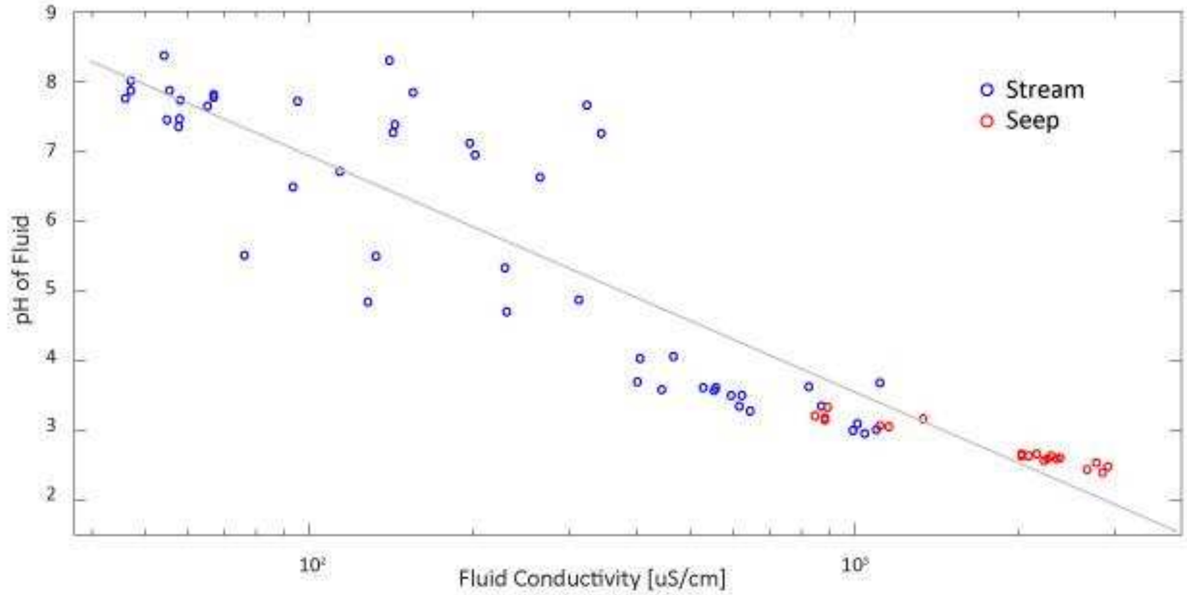

Figure 1.3: Relation between pH and log conductivity. The linear trend shown follows the equation: $pH = -3.1 * log10(\sigma_f) + 13$. The trend has an R^2 value of 0.78 and is significant with 99% confidence. The seep and stream data points overlap in the high σ_f, low pH range, indicating that the relationship between σ_f and pH is similar for seep and stream water.

The goals of this project are to characterize the flow of AMD from Minnesota Mine to Lion Creek, to identify discrete and diffuse sources of AMD impacting Lion Creek, to investigate seasonal variation in AMD contribution levels, and finally to inform ongoing remediation efforts. The results of this project were compiled into a manuscript for submission to the journal *Mine Water and the Environment*, presented in the next chapter.

CHAPTER 2

AN INTEGRATED GEOPHYSICAL AND GEOCHEMICAL APPROACH TO CHARACTERIZING ACID MINE DRAINAGE IN A HEADWATER MOUNTAIN STREAM IN COLORADO, USA

A paper to be submitted to *Mine Water and the Environment*

Allison Johnston[1], Robert L. Runkel[2], Alexis Navarre-Sitchler[3], Kamini Singha[4]

2.1 Abstract

This study integrates geochemical sampling, fluid electrical conductivity (σ_f) logging, electromagnetic induction (EMI), and electrical resistivity imaging (ERI) to investigate the impact of acid mine drainage (AMD) from the Minnesota Mine, an inactive gold and silver mine, on Lion Creek, a headwater mountain stream near Empire, Colorado. The study goal is to assist in evaluating remediation options by characterizing seasonal variation in AMD contamination levels and identifying the controls of point and diffuse sources of AMD entering Lion Creek. The pH and log (σ_f) of the water in Lion Creek inversely correlate, indicating that the low pH characteristic of AMD-impacted water correlates to high σ_f values that can serve as a target for the geophysical methods. ERI surveys were run along the east bank of Lion Creek along a reach where acidic water seeps out of the steep stream bank and into the creek. These ERI surveys identified two areas where diffuse contamination is likely entering the stream: (1) the subsurface extent of two seepage faces visible on the surface and (2) runoff leaching through a tailings pile on the east bank of Lion Creek. σ_f in the stream was lowest when the stream level was highest in the early summer and then increased throughout the summer as the stream level decreased, indicating that the concentration of dissolved solids in the stream is largely controlled by dilution due to snowmelt. Total

[1] Primary Author and Researcher, Graduate Student, Colorado School of Mines
[2] Scientist, US Geological Survey Toxic Substances Hydrology Program
[3] Assistant Professor, Colorado School of Mines
[4] Associate Professor, Colorado School of Mines

dissolved solids (TDS) were calculated using an empirical relationship between σ_f and TDS, and TDS load (TDS concentration times stream discharge) was calculated. TDS load is greatest in the early summer and displays a large diel signal. This work will be helpful in informing remediation efforts because the identification of diffuse sources of AMD allows for more targeted remediation options and knowledge of seasonal variation is necessary in predicting the costs and outcome of different remediation scenarios.

2.2 Introduction

The Colorado Mineral Belt is home to thousands of inactive mines, a result of historic gold and silver rushes (e.g., Lovering and Goddard, 1950), and there are many more across the United States (e.g., Evangelou and Zhang 1995). These mines may pose an environmental threat as water drains through mine workings and tailings piles that commonly contain metal sulfide minerals (e.g., Chandra and Gerson 2010). This exposes the metal sulfide minerals, the most common being pyrite, to a weathering environment. When metal sulfides oxidize, they release large amounts of acidity, mobilizing low pH, metal-rich water, called acid mine drainage (AMD) (Moses and Herman 1989; Moses and Herman 1991; Evangelou and Zhang 1995; Johnson and Hallberg 2005; Chandra and Gerson 2010; Nordstrom 2011). Acid rock drainage occurs naturally as rock containing metal sulfides weathers. This process is anthropogenically enhanced when valuable minerals contained in metal-sulfide rich ore are mined (e.g., Nordstrom 2011). Mining exposes the metal sulfides to weathering and increases its surface area available for reaction, which enhances its oxidation, producing AMD (e.g., Banks et al. 1997).

AMD is detrimental to water quality; the pyrite oxidation reaction releases proton acidity that often lowers the pH of surface water to values around 2 (Evangelou and Zhang 1995; Hazen et al. 2002; Johnson and Hallberg 2005; Hallberg 2010). At these low pH values, metal solubility increases, causing metals contained in the ore to mobilize in the environment. Iron, aluminum, manganese and copper are often dissolved in AMD water as well as metalloids such as arsenic, although the species present depend on the mineralogy of the site (Akcil and Koldas 2006; Nordstrom 2011). Once the pH of the water body rises, generally through mixing with fresh water, the dissolved metals begin to precipitate, with the most abundant precipitate being iron oxide. The combination of low pH, high metal concentrations and metal oxides deposited on the stream bed results in high stress on the lotic ecosystem, leading to reductions of macroinvertebrate abundance and diversity as well in changes in composition of the algal community (DeNicola and Stapleton 2002; Niyogi et al. 2002). The US Bureau of Mines estimates that AMD has adversely affected 19,000 km of streams and rivers and 700 km^2 of lakes and reservoirs (e.g., Evangelou and Zhang 1995).

Effective remediation of these sites requires extensive site characterization, including a detailed spatial distribution of AMD sources, which can be categorized as either discrete or diffuse. Additionally, information about metal loading (the amount of metals passing through the stream per time) and its seasonal and diel variation is needed because shifts in water quality are sometimes so great that a site exceeds regulatory standards for only part of the day or year (e.g., Kimball et al. 2006; Kimball et al. 2010; Nordstrom 2011). Common methods of AMD site characterization are hydrologic tracer techniques (e.g., Bencala and Walters 1983) combined with synoptic sampling, which provides a detailed spatial profile of discharge and AMD contaminant concentration along the study catchment. This information can then be used to determine incremental and cumulative metal loading along the study reach, to identify sources, and then to generate a reactive transport model (Kimball et al. 2002; Caruso et al. 2008; Butler et al. 2009; Runkel et al. 2012; Runkel et al. 2013).

While discrete sources are typically easy to identify with synoptic sampling, diffuse sources are more difficult to detect and can contribute a significant contaminant load (Banks and Palumbo-Roe 2010). Diffuse sources include contaminated groundwater entering the stream in gaining reaches, entrainment of metal-rich sediment, re-dissolution of metals that had previously precipitated, and storm runoff from mine spoils (Gozzard et al. 2011; Nordstrom 2011). Baresel et al. (2006) constructed a catchment-scale costminimization model for a river in Sweden impacted by AMD and found that information about the spatial distribution of point and diffuse AMD sources is critical for spatially targeted, cost-effective remediation measures.

Another challenge in site characterization prior to remediation is the characterization of seasonal variation in the concentration and load of AMD constituents. Stream hydrographs in the Rocky Mountains are generally snow dominated, with as much as 80% of annual precipitation originating as snowmelt (Baron and Campbell 1997; Brooks et al. 2001). Snowmelt sometimes drives a spike in the concentration of AMD constituents at the beginning of spring runoff, known as 'first flush' (e.g., Hornberger et al. 1994; Boyer et al. 1997; Brooks et al. 2001; Nordstrom 2009; Nordstrom 2011). This behavior is commonly seen in dissolved organic carbon concentrations; however, Brooks et al. (2001) found that zinc concentrations showed an annual first flush in catchments that were mining impacted. Conversely, zinc concentrations were diluted during snowmelt in neighboring catchments containing elevated metal concentrations due to disseminated pyrite, but undisturbed by mining. Hornberger et al. (1994) and Boyer et al. (1997) describe the first flush mechanistically as the result of water table rise during spring melt, which flushes out chemical species that built up in pore water during late summer to fall. Additionally, water table rise may result in a hydrologic connection between the stream and mine waste that was previously disconnected (Brooks et al. 2001). After the first flush, species tend to be diluted by the increased runoff, resulting in a rapid decline in concentrations during high, early-summer discharge periods (Butler et al. 2008; Kimball et al. 2010). In other words, there are often high concentrations during the rising limb of the stream hydrograph followed by declining concentrations during the falling limb of the stream hydrograph (Boyer et al. 1997; Brooks et al. 2001).

The extent of first flush behavior of AMD constituents as well as seasonal variation in hardness concentrations varies even between mining impacted snow-dominated systems, causing highly site specific patterns in loading and toxicity. Three studies illustrating different seasonal concentration regimes are highlighted. Kimball et al. (2010) found that the concentrations of iron, manganese and zinc in the Animas River in Southwestern Colorado were similar throughout the year, so metal loading was highest when flow was highest. However, calcium and magnesium concentrations were diluted during high flows, resulting in an increased hardness-based toxicity during high flows even though concentrations were lower. August and others (2002) found that iron, manganese and zinc concentrations in a tributary of the Arkansas River near Leadville, CO spiked during early snowmelt because of runoff from a tailings pile that only entered the study stream during high flows. This also results in the highest metal loading during high flows. In a study in the River West Allen catchment in the UK, Gozzard et al. (2011) recorded decreased manganese and zinc concentrations with increasing flow, but iron concentration increased with increasing flow. This result was likely because at their site, high flows produced more surface runoff, which joined the study reach by way of iron-rich peat bogs. In this case, the manganese, zinc and iron metal loads were also highest during high flows. Consequently, while the metal load of common AMD constituents is often higher in high flow regimes, it is important to understand the site specific factors that cause temporal variation in concentration and source of major AMD constituents as well as hardness levels which can affect the toxicity of metal contaminants.

Several studies have found that the relative contribution of AMD constituents from point and diffuse sources varies seasonally as well as concentrations and loads of AMD constituents. For example, during low flows, Gozzard et al. (2011) found that 60.9% of the total zinc was from one of three point sources. During high flows, only 6.8% of total zinc was from point sources. Importantly, the study concluded that even if all the point sources were treated, the catchment is unlikely to meet regulatory goals for water quality. Likewise, Kimball et al. (2010) found that the contribution of point sources was much greater during low flows than high flows. The results from these studies emphasize the importance of diffuse sources of contamination as well as seasonal variation in contamination sources.

There are limited methods for investigating diffuse contamination in AMD-impacted streams, although geophysical methods show promise. Electrical resistivity imaging (ERI) and electromagnetic induction (EMI), in particular, are frequently used in environmental geophysics applications where a contaminant of interest can be identified by elevated total dissolved solids (TDS). Elevated TDS causes elevated fluid electrical conductivity ($\sigma_{f,}$), which then increases bulk electrical conductivity (σ_b). ERI resolves σ_b with depth along a survey line while EMI measures the average σ_b of the shallow subsurface and can be used to quickly map σ_b in plan view.

ERI has been used to map σ_b specifically for AMD site characterization in numerous previous studies. For example, Ebraheem et al. (1990) measured σ_b using ERI, leveraging the increased σ_f of TDS mine water to identify three valleys in which mine spoil was deposited during mining operations. Rucker et al. (2009a) used ERI to identify the most contaminated areas at an abandoned mine site. They also identified a fracture that they hypothesized transported AMD-impacted water from mine spoils to a perennial stream. Martìn-Crespo et al. (2011) used ERI to examine the geometry of mine ponds, looking for infill thickness and leaks. The investigators supplemented this work with mineralogical and geochemical data describing the composition of mine ponds so that they could estimate potential pollution in the event of a release. This research, and others (e.g., Buselli and Lu, 2001; Ramalho et al., 2009), has demonstrated the utility of ERI as a non-invasive, cost-effective site-investigation technique for AMD-impacted sites. Here, we leverage this success in past studies for our field site.

EMI has also been used to investigate AMD sites by many investigators (e.g., Buselli et al., 1998; Ladwig, 1983; Smith et al., 2007), often in combination with ERI techniques (e.g., Buselli and Lu 2001; Ramalho et al. 2009). Ladwig (1983) used EMI to compile a σ_b map that was correlated with existing well logs and used to delineate areas affected by AMD. At the larger scale, helicopter EMI surveys have been run above the AMD-impacted Animas River watershed to infer groundwater flow paths and delineate geologic features, and used as part of a larger study to inform remediation efforts in the area

(Smith et al. 2007). The main advantage of EMI is its ability to quickly resolve small variations in σ_b. In this study, we use EMI to attempt to map AMD flow paths underneath a large open field between the mine and stream.

This study takes place in the Empire Mining District, located approximately 100 km west of Denver, CO. The area has a history of gold and silver mining dating back to the late 1800s. Here, we explore the impacts of Minnesota Mine on Lion Creek, a small headwater mountain stream (Figure 2.1). Lion Creek's hydrograph is dominated by the pulse of spring runoff due to snowmelt at higher elevations. We combine geophysical and geochemical techniques to characterize the transport of AMD from Minnesota Mine to nearby Lion Creek. We use ERI, EMI, and fluid sampling to explore how and how much AMD was entering the stream from June to October, from snowmelt to the late-summer drying-out period. Our goals are multifold: (1) to characterize the inputs of AMD from Minnesota Mine to Lion Creek, (2) determine how the concentration of key AMD constituents in the creek changes seasonally, and (3) identify potential diffuse sources of contamination entering Lion Creek. We then evaluate the utility of this type of characterization in remediation design.

2.3. Background

This study fits into a rich literature of environmental geophysics methods and applications as well as the immense body of AMD site investigation literature. This study, as well as a study done in parallel by the USGS are the first to focus on Minnesota Mine and its impact on Lion Creek, though the methods employed are well represented in literature.

2.3.1 Field Site

Minnesota Mine and Mill is a historic gold mine located 2 km northwest of the town of Empire, Colorado in Clear Creek County (Figure 2.1). The gold ore found in Minnesota Mine is almost all the pyritic gold type, making it likely to produce AMD (Lovering and Goddard 1950; Cunningham et al. 1994). The veins of the mine are in the Precambrian Boulder Creek Granite formation on the northwest side of a 300-m in diameter stock of monzonite porphyry (Lovering and Goddard 1950; Braddock 1969; Cunningham et al. 1994). Although the mine is not well mapped, it is reported to have followed the veins northeast (Braddock 1969).

The mine is east of Lion Creek, a small headwater mountain stream (Figure 2.1). There is one outlet to the mine, a cement structure filled with water, located at an elevation of 2963 m. Downgradient of the mine outlet there are several seepage faces where water seeps out of the steep east streambank and then enters Lion Creek (Figure 2.1). Three major seepage faces are visible on the east bank of Lion Creek. In these areas, the steep east stream bank of Lion Creek appears to intersect the water table, and water is visibly seeping out of the stream bank at its lower portions. The seep locations in this work are described by their position in the study reach, with 0 being the farthest upstream point investigated, at an elevation of 2961 m (Figure 2.1). The first seep, called the '180-m seep,' goes from 175 m to 183 m along the study reach. It has an average pH of 3.2. The '240-m seep' occupies a large eroded area, where water with an average pH of 2.6 seeps out of the steep streambank from about 238 m to 250 m along the study reach. The '330-m seep' is located from 328 m to 335 m. The water seeping out of the stream bank here has an average pH of 2.4. Because of the presence of the seeps and their low pH, Lion Creek is suspected to be hydrologically connected to Minnesota Mine. The average elevation of the field above the mine adit is 2932 m, while the average elevation of the 180-m seep is 2921 m, the average elevation of the 240-m seep is 2908 m, and the average elevation of the 330-m seep is 2897 m. Therefore, the topographic relief between the field and the surface seeps is at least 11 m, and in some places much more. Orange iron precipitate coats the stream bed beginning upstream of the acidic seeps, indicating that there is contamination entering Lion Creek through pathways other than the visible seepage faces.

Minnesota Mine and the immediately adjacent section of Lion Creek are part of the Clear Creek/Central City Superfund Site. In 1995, the US Forest Service (USFS) entered a cooperative agreement with the Environmental Protection Agency (EPA) to clean up the 28,000 m^2 Minnesota Mine tailings property that it manages (Dodson 2004). The chief concern was sediment loading from the tailings pile entering Lion Creek after storm events, as well as cadmium, copper, zinc, iron and manganese concentration exceeding State of Colorado Table Value Standards (Looby 1991). Clear Creek is a drinking water source for a quarter of a million people in the Denver area and a major recreation area, so water quality is a major concern (Sims and Guerra 2014). The area directly below the mine outlet was graded, capped, and seeded for erosion control in November 1996 (Dodson 2004). The erosion control, reseeding, and removal of tailings have ameliorated the problem of sediment entering Lion Creek and being carried downstream. However, Lion Crook still appears to be impacted by Minnesota Mine, as evidenced by tailings on the east bank of Lion Creek and the orange and white precipitate coating the stream bed in large areas. The USFS is, as of summer 2015, planning an additional remediation that will more directly address water quality in Lion Creek.

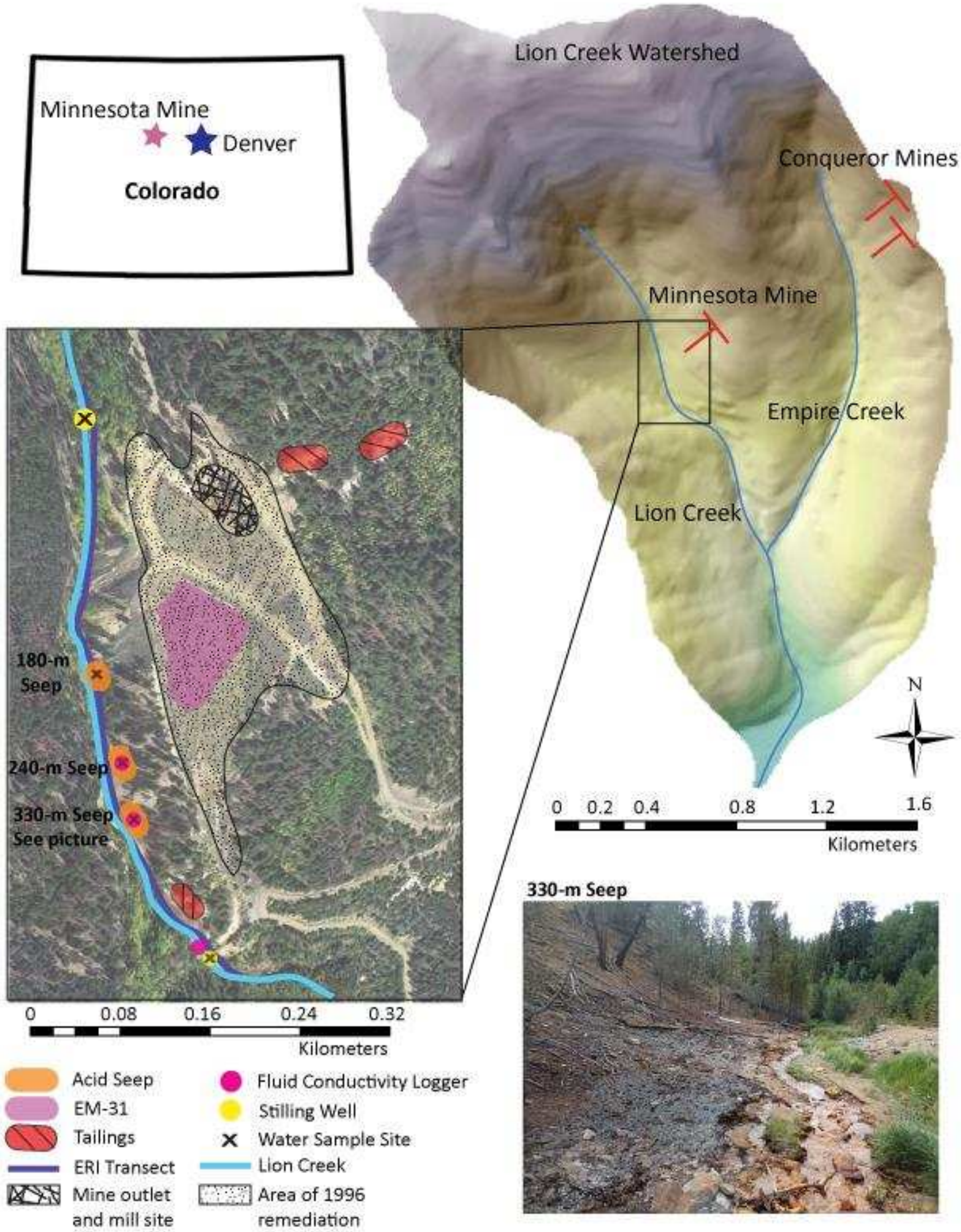

Figure 2.1: Overview of field site and instrumentation locations.

2.3.2 Acid Mine Drainage Chemistry

The oxidation of metal sulfides is the main cause of AMD. Pyrite is the most abundant sulfide mineral in the world and is often found with valuable minerals such as gold, silver, copper, and uranium (Evangelou and Zhang 1995). This makes the oxidation of pyrite the biggest contributor to AMD. Pyrite oxidation releases protons, sulfate, and ferrous iron (e.g., Banks et al. 1997; Johnson and Hallberg 2005; Nordstrom 2011). The two most common pyrite oxidation reactions are:

$$FeS_2(s) + 14\ Fe^{3+} + 8H_2O \rightarrow 15Fe^{2+} + 2SO_4^{2-} + 16H^+ \qquad (2.1)$$

$$FeS_2(s) + 7/2O_2 + H_2O \rightarrow Fe^{2+} + 2SO_4^{2-} + 2H^+. \qquad (2.2)$$

In most mine environments, pyrite oxidation by ferric iron (Equation 2.1) is much faster than oxidation by dissolved oxygen (Equation 2.2) (Taylor et al. 1984; Moses et al. 1987) due to more favorable molecular orbital conditions (Luther 1987) and the microbially mediated oxidation of ferrous iron that resupplies ferric iron (e.g., Evangelou and Zhang 1995). Although the mechanism and kinetics of pyrite oxidation are not fully understood, it is generally accepted that the reaction is a chemically controlled surface reaction, which explains why mining enhances pyrite weathering by increasing the surface area of pyrite exposed to a weathering environment.

2.3.3 Concentration-Discharge Relationships

Many previous studies have investigated the relationships between individual constituent concentrations in a stream and discharge. These relationships can be used to help understand the seasonal variation in constituent levels, predict constituent concentrations at various stream discharge levels (Malan et al. 2004), identify the source of a constituent in the stream (McDiffett et al. 1989), or to understand the underlying processes that control the concentration of the constituent (Godsey et al. 2009). A common mathematical form of the concentration-discharge relationship is

$$C = aQ^b + C_0 \qquad (2.3)$$

where C is the constituent concentration [mg/L], C_0 is the concentration of that constituent entering the stream [mg/L], Q is the stream discharge [L/s] and a and b are empirical constants related to the relationship between stream discharge and volume of water in the stream channel (Hall 1970; Hall 1971). In this case, a log-log plot of discharge and concentration is a straight line if the inflow concentration is steady in time (Hall 1971). If the slope of the linear trend is -1, the relationship is perfectly dilution controlled. A slope of zero indicates chemostatic behavior, meaning that the catchment system keeps the concentration of solutes constant, potentially as a result of attenuation processes in the stream, or inputs to the stream which have a similar concentration as the stream (Godsey et al. 2009).

2.3.4 Electrical Resistivity Imaging

ERI is used to create a 2D (and sometimes 3D) map of σ_b in the shallow subsurface beneath a row of electrodes. In this method, direct current is transmitted through one pair of electrodes, called the transmitting dipole. The resulting potential is measured across a second pair of electrodes, called the receiving dipole. Each measurement at a distinct electrode configuration is known as a quadripole. The electric potential of a continuous medium as the result of a point source of current can be described by Poisson's Equation (e.g., Binley and Kemna 2005; Day-Lewis et al. 2005; Rucker et al. 2009b; Loke et al. 2013):

$$-\nabla \cdot \sigma_b \nabla \phi = I\delta(x - x_s,\ y - y_s, z - z_s) \qquad (2.4)$$

where σ_b is bulk electrical conductivity [S/m], ϕ is electrical potential [V], I is electrical current source [A], (x,y,z) is the position in space [m], (x_s,y_s,z_s) is the position of current source [m], and δ is the delta function. This equation relates the electrical potential distribution in a medium to the σ_b distribution. Because the field data collected using ERI consists of a limited number of potentials and currents, an inverse method, described below, must be used to estimate a σ_b model that explains the electrical potential data.

2.3.4.1 Inversion

Due to practical limitations on the amount and accuracy of data collected, the inverse problem is inherently ill-posed, meaning many models may fit the field data with the same level of data misfit (Binley and Kemna 2005). ERI inversion, or image reconstruction of σ_b maps of the subsurface, is often done using an Occam's inversion scheme. An Occam's inversion choses the solution with a specified level of data misfit and the least complex structure; it is named after the heuristic technique Occam's Razor (deGroot-Hedlin 1990; LaBrecque 1996). The inverse problem is set up as an optimization problem, in which an objective function is minimized:

$$\Psi(\boldsymbol{m}) = \|\boldsymbol{W_d}[\boldsymbol{d} - \boldsymbol{f}(\boldsymbol{m})\|^2 + \alpha \left\|\boldsymbol{W_m}[\boldsymbol{m} - \boldsymbol{m_{ref}}\right\|^2 \qquad (2.5)$$

where the first term on the right hand side is the data misfit term, and the second is the reference model term. In Equation 2.5, $\boldsymbol{W_d}$ is the data weighting matrix, **d** is the data vector, $\boldsymbol{f}(\boldsymbol{m})$ is the forward model of the model vector **m**, α is the weight that controls the relative importance of the data misfit and reference model terms of the objective function, $\boldsymbol{W_m}$ is the model weighting matrix, and $\mathbf{m_{ref}}$ is the reference model (Binley and Kemna 2005).

The measured electrical potentials normalized by the injected current are contained in the data vector **d**. The data misfit term uses the data weighting matrix $\boldsymbol{W_d}$ to specify the weights of each data point. Often, and in this study, the reciprocal of the standard deviation of the stack for each quadripole is used. The model objective function imposes model constraints using the reference model $\mathbf{m_{ref}}$ and the model weighting matrix $\boldsymbol{W_m}$, which enforces the model's smoothness in its departures from the reference model using the second derivative of the modeled σ_b. The weight α controls the relative importance of the data misfit and reference model terms of the objective function. The value of α is minimized during each iteration as in deGroot-Hedlin and Constable (1990) so that the model is penalized more for data misfit than for roughness.

In the inversion algorithm, the distribution of electrical properties is discretized into a set of log transformed σ_b parameters that make model vector **m**. The reference model $\mathbf{m_{ref}}$ serves as a starting point for the algorithm. The reference model can be a set of expected parameter values, a previous inversion, or a homogeneous halfspace if there is no information available. The objective function, Equation 2.5, is minimized using a gradient search method. This is included in a Gauss-Newton iteration scheme, which is set up as shown in Equations 2.6 and 2.7 (Binley and Kemna 2005):

$$\left(\boldsymbol{J}_k^T\boldsymbol{W}_d^T\boldsymbol{W_d}\boldsymbol{J}_k + \alpha\boldsymbol{W}_m^T\boldsymbol{W_m}\right)\Delta\boldsymbol{m}_k = \boldsymbol{J}_k^T\boldsymbol{W}_d^T\boldsymbol{W}_d[\boldsymbol{d} - \boldsymbol{f}(\boldsymbol{m}_k)] - \alpha\boldsymbol{W}_m^T\boldsymbol{W}_m(\boldsymbol{m}_k - \boldsymbol{m}_{ref}) \quad (2.6)$$

$$\boldsymbol{m}_{k+1} = \boldsymbol{m}_k + \Delta\boldsymbol{m}_k \quad (2.7)$$

where $\boldsymbol{J}_k$ is the Jacobian matrix for the current iteration step, as defined by:

$$J_{ij} = \frac{\partial d_i}{\partial m_j}. \quad (2.8)$$

During each iteration step, Equation 2.6 is solved for $\Delta\boldsymbol{m}_k$, which is used as in equation 2.7 to update the model. This process is repeated until $\Psi_d(\boldsymbol{m}_k)$ matches the target data misfit value (Binley and Kemna 2005).

The target data misfit for the inversion is 1.0, since as shown in Equation 2.5, the root-mean-square data misfit is normalized by the standard error of each measurement point. Occam's inversion schemes are sensitive to the noise level of the data used in the inversion, so it is important that the model weighting matrix contains measurements that accurately reflect the actual standard deviation of the data (LaBrecque 1996). Assuming the standard deviation of the stack at each quadripole is representative of the noise for each measurement, a model that is fit to a smaller than actual data misfit will result in an image that is unnecessarily rough or includes structures that do not exist in the true section (LaBrecque 1996). If the model is fit to a larger than actual data misfit, it will reduce the resolution of the image and possibly smear geologic features. This scheme only addresses Gaussian noise in the data; it does not account for systematic errors. Systematic errors are potentially generated by electrodes that are slightly out of place, distortion by 3D structures that are unaccounted for in the 2D representation of the subsurface, or poor electrode contact (LaBrecque 1996; Binley and Kemna 2005).

There are several ways to evaluate the inversion model results. In particular, the resolution matrix **R** is often used because it gives a quantitative representation of the model's resolution, which is affected by the σ_b of the subsurface, the geometry of the survey, the inversion parameterization and regularization, and error in the survey measurements (e.g., Day-Lewis et al. 2005). The resolution matrix is calculated according to (e.g., Binley and Kemna 2005; Day-Lewis et al. 2005):

$$\boldsymbol{R} = \left(\boldsymbol{J}_k^T \boldsymbol{W}_d^T \boldsymbol{W}_{\boldsymbol{d}} \boldsymbol{J}_k + \alpha \boldsymbol{W}_m^T \boldsymbol{W}_{\boldsymbol{m}}\right)^{-1} \boldsymbol{J}_k^T \boldsymbol{W}_d^T \boldsymbol{W}_d \boldsymbol{J}_k \qquad (2.9)$$

$$\boldsymbol{m} \cong \boldsymbol{R}\boldsymbol{m}_{true} \qquad (2.10)$$

As per equation 2.10, any deviations in **R** from the identity matrix indicate the effects of regularization, and can be used to identify areas of the image that could contain artifacts (e.g., Binley and Kemna 2005; Day-Lewis et al. 2005).

Another way to evaluate the meaningfulness of the inversion model is to look at how strongly the starting model effects the final resistivity model, for example, using the Depth of Investigation (DOI) method of Oldenburg and Li (1999). In the DOI method, the same data set is inverted using a high and a low σ_b homogeneous reference model. The resulting models should be the same if they are independent of the reference model chosen. The DOI index is calculated for each cell in the final σ_b model to determine how strongly the final model is affected by the reference model:

$$DOI(x,z) = \frac{1/\sigma_{b1}(x,z) - 1/\sigma_{b2}(x,z)}{1/\sigma_{b1r} - 1/\sigma_{b2r}} \tag{2.11}$$

where σ_{b1r} is the value of the low σ_b homogeneous reference model, σ_{b2r} is the value of the high σ_b homogeneous reference model, and $\sigma_{b1}(x,z)$ is the σ_b of the model cell at (x,z) using the inversion starting with the low σ_b reference model. The DOI index should equal zero if the final σ_b model is not affected by the reference model.

2.3.4.2 Time-Lapse ERI

Many studies use time-lapse ERI, in which multiple sets of measurements are collected over the same survey transect throughout time. This technique is common in tracer studies because any changes in σ_b can be attributed to changing σ_f due to the tracer. This allows separation of the effects of geologic features on σ_b from the effects of parameters changing due to hydrologic processes, such as variation in moisture content or σ_f on σ_b. Tracer studies in conjunction with time-lapse ERI have been used to estimate transport parameters in a heterogeneous aquifer (e.g., Kemna et al. 2002), investigate hydrologic connection between two aquifers (e.g., Cassiani et al. 2006), and characterize stream-hyporheic zone dynamics (e.g., Ward et al. 2010; Ward et al. 2014). Time-lapse ERI is less common in AMD site investigations studies because the high background σ_f makes it difficult to use a tracer to raise σ_f high enough above background levels to confidently image tracer induced changes in σ_b. A recent study by Bethune et al. (2015) circumvented this issue by using the change in pore water σ_f due to snowmelt as a tracer. They did a time-lapse ERI survey along Peru Creek, another mining impacted stream in the Colorado Mineral Belt, from June to October. The survey showed conductive anomalies becoming less conductive throughout the summer as the σ_f of mine impacted pore water decreased. This allowed them to hypothesize that there were preferential flow paths between Pennsylvania Mine and Peru Creek.

Time-lapse ERI inversions are generally done using difference inversion, meaning that the inversion scheme starts with a background σ_b model, typically from data collected before the tracer is introduced, and only needs to find differences in σ_b from the background for each subsequent data set. This allows difference inversions to converge faster and reduces systematic errors in the modeled perturbations from the background σ_b model, such as errors pertaining to electrode placement and the discretization method used (LaBrecque and Yang 2001). However, difference inversion does not reduce error in the actual σ_b model, only in the modeled percent change in σ_b.

2.3.5 Electromagnetic Induction

For this study, the EMI data were collected using a Geonics EM31 (Geonics Limited, Mississuaga, Ontario, Canada) with a Polycorder 600 datalogger. The EM31 has two coplanar coils spaced 3.7 m apart. The coils can be operated in either horizontal or vertical dipole mode. The transmitting coil induces a primary alternating magnetic field, which induces a small current in the earth between the transmitting and receiving coils. The induced current then induces a secondary magnetic field. The receiving coil senses the primary and the secondary magnetic fields (Tezkan 1999). The EM31 has an operating frequency of 9.8 kHz and an expected depth of investigation of about 6 m in the vertical dipole mode (Tezkan 1999). The EM31 uses a 'Slingram Method,' in which both the in-phase and 90 degrees out-of-phase, or quadrature, components of the magnetic fields are measured. The quadrature measurement is linearly related to σ_b and is sensitive to small lateral changes in σ_b (McNeill 1980). The in-phase component is often used to detect metal since it is not sensitive to small changes in σ_b, but does respond to discrete conductive bodies with a large deflection from background signal values (McNeill 1983).

High σ_b can invalidate the low induction number assumption, meaning that the measured σ_b begins to be lower than the true σ_b (McNeill 1980; Tezkan 1999). The induction number is the ratio between the intercoil spacing, which is fixed at 3.7 m for the EM31, and the skin depth (δ). The skin depth is the depth at which the amplitude of the electromagnetic field drops by a factor of 1/e compared to the original amplitude (McNeill 1980):

$$\delta = \sqrt{\frac{2}{\omega\mu_0\sigma_{ba}}} \tag{2.12}$$

where ω is the angular frequency [s^{-1}], μ_0 is the permeability of free space [ohm s m^{-1}], and σ_{ba} is the apparent σ_b [S/m]. Therefore, the higher the σ_b**,** the higher the induction number. In the case of a skin depth much greater than the intercoil spacing, and therefore an induction number much less than one, the ratio of the quadrature component of the secondary magnetic field to the primary magnetic field can be linearly related to σ_{ba}:

$$\sigma_{ba} = \frac{4}{\omega\mu_0 s^2}\frac{H_s}{H_p} \tag{2.13}$$

where H_s is the secondary magnetic field [A m^{-1}], H_p is the primary magnetic field [A m^{-1}], s is the intercoil spacing [m], and δ is the skin depth [m]. The low induction number assumption begins to breakdown at about 100 mS/m.

2.3.6 Relating Bulk Electrical Conductivity and Fluid Electrical Conductivity

Archie (1942) describes the relationship between the σ_b of a saturated porous media and the σ_f of its pore water as $\sigma_b = F\sigma_f$, where F is the formation factor, which is a function of effective porosity and tortuosity. This relationship was developed for sandstone formations with no clay content and therefore little cation exchange capacity (CEC). In media containing clays or shales, negative surface charges cause cations to accumulate near the sediment surface, resulting in the formation of an electrical double layer (e.g., Sen et al. 1988) . Current conducts along the electrical double layer as well as through the pore fluid, causing an increase in the measured σ_b of the porous medium. Several other researchers have updated Archie's relationship to address the surface conductance of the porous medium. For example, the empirical relationship between σ_b and σ_f proposed by Sen et al. (1988) is:

$$\sigma_b = \frac{S_w^n}{F}\left(\sigma_f + \frac{1.93nQ_v}{1+0.7/\sigma_f}\right) \tag{2.14}$$

where S_w is the water saturation of the porous media, n is the saturation exponent (usually close to 2), and Q_v is the excess surface charge per unit volume [eq/L] (e.g., Waxman and Smits 1968; Revil et al. 1998).

2.4 Methods

This study uses four main methods to characterize the impacts of AMD on Lion Creek: ERI, EMI, water sampling, σ_f logging and stilling wells. ERI was used to resolve the σ_b of the shallow subsurface and to investigate subsurface geologic structure along Lion Creek. EMI was used to survey large areas quickly and to form plan-view maps of the depth averaged σ_b in the areas between the mine and the creek, with the goal being to map subsurface flowpaths in the 11- to 14-m thick section of material from the mine to the stream. Water sampling was used to find the concentrations of individual AMD constituents to help interpret the σ_f measurements. σ_f logging was used to collect a continuous time series of stream and seep σ_f to monitor how much AMD was entering the stream over the same time. Finally, stilling wells were used to continuously measure stream stage, converted to discharge using a rating curve. The location of each measurement site is shown in Figure 2.1. Additionally, precipitation and snow water equivalent (SWE) data were taken from SNOTEL site on Berthoud Summit, approximately 6.5 km northwest of Minnesota Mine. These data were used to investigate the response of the stream TDS to precipitation and snowmelt.

2.4.1 Electrical Resistivity Imaging

Replicate ERI data sets were collected on a transect that roughly parallels Lion Creek at two-week to one-month intervals from May 12 to October 2, 2015. The ERI transect parallel to the stream was composed of 96 stainless steel electrodes placed at 5-m intervals for a total line length of 480 m. The ERI data were collected using a dipole-dipole sequence, which has an independent transmitting and receiving dipole and is sensitive to near-surface changes (Binley and Kemna 2005). Each survey included 1,829 quadripoles. Each quadripole measurement is the average of three to six stacked measurements, and a coefficient of variation was calculated at each quadripole for the stacked measurements. A Syscal Pro resistivity meter (IRIS Instruments, Orleans, France) was used to collect the measurements. Additional ERI data were collected across the large field directly south of the mine workings where replicate EMI data sets were collected, shown in Figure 2.1.

For the ERI transect parallel to the stream, a finite-element mesh was created to parameterize the model using 1.25-m spacing in the x-direction along the stream, resulting in four boxes in between adjacent electrodes. The mesh was spaced at 1-m intervals in the z-direction down to 10 m. Larger pixels were used at the edges to push the lateral and vertical boundary conditions away from the area of interest. The resistance data were inverted using R2 version 2.7a, described by Binley and Kemna (2005). The reference model for the first dataset collected 12 May was a homogeneous halfspace with a σ_b of 10 mS/m, approximately equal to the average apparent σ_b of the dataset before the correction for the elevation of each electrode. Each subsequent dataset was inverted twice, using the 12 May inversion as well as a homogeneous halfspace for a reference model. The DOI index was calculated using a low reference model of 2 mS/m and a high reference model of 20 mS/m for each cell in the final σ_b model. The image transparency was increased for cells with DOI indices greater than 0.4.

2.4.2 Electromagnetic Induction

EMI data were collected in a large field directly south of the outlet of the mine adit (Figure 2.1). The datalogger was set up to record in-phase and quadrature measurements at a half-second time interval. All measurements were collected in vertical dipole mode due to its deeper depth of investigation when compared to the horizontal dipole mode. Data were collected by walking across the field in lines spaced 5 m apart. The quadrature data were used to create a σ_b map of the area, and the in-phase data were used to identify subsurface metal structures.

2.4.3 Water Sampling

Water samples were taken in July and August at five sites to corroborate the σ_f data: Upper Lion Creek, the seep at 180 m from the top of the research reach, the seep at 240 m, the seep at 330 m and Lower Lion Creek (Figure 2.1). Two 60 mL samples were taken at each site. Both samples were filtered with a 0.45 micron filter so that only dissolved species would be present. The samples analyzed for cations were acidified using trace metal grade nitric acid so that the metals present would stay in solution. The samples analyzed for anions were not acidified. All samples were refrigerated before they were analyzed. The samples were analyzed for cations using inductively coupled plasma atomic emission spectroscopy and for anions using an ion chromatograph. Geochemist Workbench (Bethke and Yeakel 2015) was used to speciate the sample results, and bicarbonate concentrations were modeled such that they were assumed to be in equilibrium with atmospheric CO_2.

2.4.4 σ_f Logging

Three Solinst Levelogger 3001 probes were deployed 1 June 2015 along the stream reach: in Lower Lion Creek, the 240-m seep, and the 330-m seep (Figure 2.1). The probes measure pressure, temperature and σ_f. Point σ_f and pH measurements were also taken by hand with a Thermo Electron Corporation Orion 4 Star portable pH and σ_f meter at every 12th ERI electrode and at sampling sites throughout the field season. The σ_f probe for the portable meter and each Levelogger were calibrated using a 1,413 uS/cm and a 12,880 uS/cm σ_f standard. The pH probe was calibrated using a pH 4.01 and 7.00 standard solution. Each probe was calibrated prior to going to the field site, and checked upon return to the laboratory. The measured σ_f were corrected to specific σ_f at 25^{0}C according to:

$$\sigma_{f,25} = \frac{\sigma_{f,m}}{1+\gamma(t_m-25)} \quad (2.16)$$

where $\sigma_{f,25}$ is the specific conductivity at 25^0C, $\sigma_{f,m}$is the measured σ_f at temperature t_m, and λ is the correction factor (Hayashi 2004; Radtke et al. 2005). A λ value of 0.0180 was used, based on previous freshwater studies (e.g., Smith, 1962).

2.4.5 Relationship of σ_f to TDS

To estimate TDS loading, the σ_f measurements were converted to TDS using the empirical relationship detailed in Ebraheem et al. (1990):

$$log10(TDS) = 1.216 * log10(\sigma_f) - 0.584 \qquad (2.17)$$

Equation 2.17 was applied successfully by Yuval and Oldenburg (1996) to data from an AMD site in Ontario, Canada, suggesting that the equation may be applied cautiously to other AMD sites. Due to potential issues in applying an empirical relationship from a different field site, the calculated TDS values were checked against the values measured in the water samples. The calculated time series of TDS was then used calculate the load of dissolved solids entering the stream (TDS*Q) throughout the field season.

2.4.6 Stilling Wells

Two stilling wells were installed in Lion Creek, one at the upstream end of the study reach and one at the downstream end. The detailed locations are shown in Figure 2.1. Each stilling well consists of a 1 m long piece of PVC with holes drilled in the side driven into the streambed and anchored with rebar on either side of the PVC. A HOBO water level logger (Onset Computer Corporation, Bourne, MA) was placed inside the PVC and set to record pressure and temperature at 20-min intervals. An additional water level logger was placed on the stream bank to record barometric pressure. The water pressures were corrected for barometric pressure and converted to stream height.

Throughout the field season, six stream velocity profiles were measured using the OTT MF Pro flow meter (OTT Hydromet, Kempton, Germany) and then converted to stream discharge using the measured cross sectional area of the stream, known as the velocity-area method. The measured stream discharge was plotted against the stream height at the stilling well, forming a rating curve. That curve was used to convert the stream heights measured at the stilling wells to a continuous record of discharge. The discharge record at the lower stilling well was poorly correlated to both the discharge measured at the upper stilling well and the discharge recorded at the USGS stream gauge in the west fork of Clear Creek, just downstream of where Lion Creek drains into Clear Creek. Because of the anomalous data as well as large amounts of iron precipitate observed on the instrument, the discharge measured at the lower stilling was discarded, and only discharge at the upper stilling was used.

2.5 Results and Discussion

The results of the extensive field campaign conducted from May to October, 2015 are compiled in this section, broken into sections for each method. We present key AMD constituent concentrations from the water samples, the time series σ_f records from the σ_f logging, and an EMI and ERI σ_b map.

2.5.1 Water Sampling

Water samples were taken to explore the concentration of individual constituents along the stream and in the acidic seeps (Figure 2.2). The shape of the stiff diagrams show the general geochemical composition of the samples. Aluminum, copper, iron, manganese and zinc are all found in higher concentrations at the Lower Lion Creek sampling site compared to the Upper Lion Creek sampling site, suggesting the metals enter the stream in the study reach. The metals are at the highest concentrations at the 180-m, 240-m and 330-m seep sampling sites. The 240-m seep, 330-m seep and Lower Lion Creek have similar geochemical compositions, while Upper Lion Creek has much lower aluminum, copper, manganese and zinc concentrations. The seepage water not only has higher metal concentrations than Lion Creek, but also higher concentrations of weathering products such as calcium, magnesium and sodium. This is likely because the water dissolves these constituents as it travels through the shallow subsurface. The 330-m seep shows the highest σ_f measurements (Figure 2.3b) and also has the highest concentration of each dissolved constituent with the exception of arsenic. The concentration of each constituent in the acidic seeps tends to increase down the study reach.

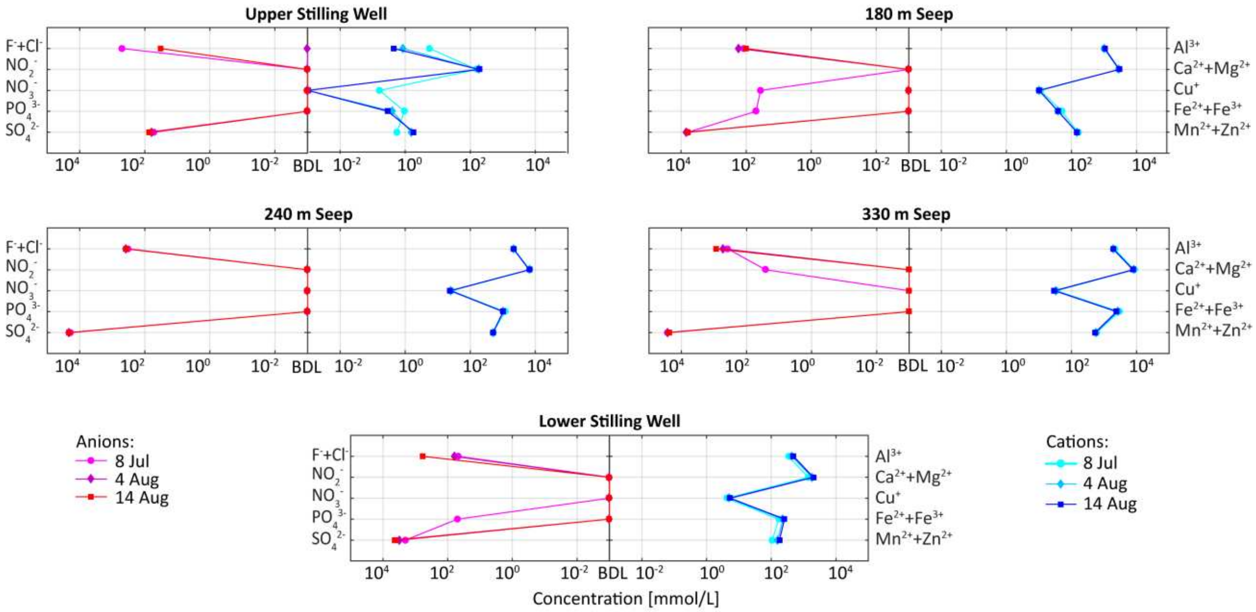

Figure 2.2: Stiff diagrams of water samples from 8 July, 2015, 4 August, 2015, and 14 August, 2015. The ionic constituents of highest concentrations are shown.

The ratio of molar sulfate concentration to molar iron concentration is sometimes used to determine how close to the AMD source respective waters are since sulfate is attenuated much slower than iron as it travels through the environment (e.g., Olías et al. 2004). Therefore, a high sulfate to iron ratio indicates that AMD water is temporally or spatially removed from the AMD source. The ratio of sulfate to iron in the products of pyrite oxidation by ferric iron (Equation 2.1) is 2:15, and in the products of pyrite oxidation by dissolved oxygen it is 1:2 (Equation 2.2) (Olías et al. 2004). The ratio of sulfate to iron was calculated at each of the sample sites for each of the three dates samples were collected. The sulfate to iron ratios indicate that the water in the 330-m seep is closest to the ratio expected for AMD, followed by Lower Lion Creek, the 240-m seep, Upper Lion Creek, and then the 180-m seep. In other words, the 330-m seep is chemically the closest seep to the AMD source, although it is the farthest from Minnesota Mine. This suggests that there may be preferential flow paths from the mine to the seep.

The concentration of each of the main constituents stays fairly constant in the seepage water between July and August with the exception of nitrate and phosphate in the 180-m seep and nitrite in the 330-m seep. In contrast, there is a notable variation in cation constituent concentration at both the Upper and Lower Lion Creek sample sites. Cation concentrations generally increase from July to August at the Lower Lion Creek sample site, likely because the input from the seeps stay fairly constant while the freshwater input from snowmelt declines.

A Geochemist Workbench model was made to speciate the sample results and to compute HCO_3^- concentration with the assumption that it is in equilibrium with atmospheric CO_2. Using the modeled results, the charge balance for the samples was calculated as a percentage of the total milliequivalents of charge per liter. The charge balance for each of the samples from the stream was less than 10%, but the charge balance for the samples from the seeps had much higher magnitudes, from 40 to 50%. This is clearly indicative of an error in the geochemical analysis, and further work is being done to address the problem. Because of this problem, the concentration of individual species in the seepage face samples is not used quantitatively in this analysis and will not be used in our conclusions.

2.5.2 σ_f Logging and Discharge

Equation 2.18 shows the empirical inverse linear relationship between log10(σ_f) and pH measurements taken in Lion Creek and in the seepage water:

$$\mathrm{pH} = -3.1 * \log 10(\sigma_f) + 13. \qquad (2.18)$$

The trend has an R^2 value of 0.78 (p-value < 0.01). The trend between log10(σ_f) and pH is supported by many previous studies (e.g., Herbert, 2006; Mighanetara et al., 2009). Equation 2.18 relates σ_f to a known product of AMD, proton acidity (Equation 2.1), thus the σ_f measurements may be used to compare the extent of AMD contamination at different locations and times. The measurements show less variation at low pH, possibly because the bicarbonate system buffers pH changes when pH is around 6.1. The buffering system damps pH changes but not σ_f changes, resulting in a range of pH values for the same σ_f. The seep and stream data points overlap in the high σ_f, low pH range, indicating that the relationship between σ_f and pH is similar for seep and stream water.

We see diel, seasonal, and event-based changes in stream σ_f (Figure 2.3). Stream stage has a strong diel signal, with lower stage during the day and higher stage at night due to evapotranspiration occurring during the day (Figure 2.3a inset). Similarly, the stream σ_f has a strong diel signal, even after it has been corrected to account for temperature variation via Equation 2.16 because the TDS concentration increases as freshwater is lost due to evapotranspiration (Figure 2.3a inset).

Seasonal variation in stream discharge drives much of the variation in stream σ_f in snow-dominated systems. Stream discharge measurements began on 19 June 2015 and continued through 23 October. Discharge declines rapidly from the beginning of its record through the middle of July, while SWE values measured at the Berthoud Summit SNOTEL site decline rapidly and reach zero by the middle of June. SWE values measured at the Berthoud Summit SNOTEL site correspond to SWE on an exposed ridge that receives more solar radiation than the densely forested gulch that Lion Creek runs through. Based on this, and field observations of snow on 23 June, Lion Creek continued to receive smaller amounts of fresh water inputs from snow melt until at least the end of June. Heterogeneous snow melt is common in forested watersheds (Elder et al. 1991; Boyer et al. 1997).

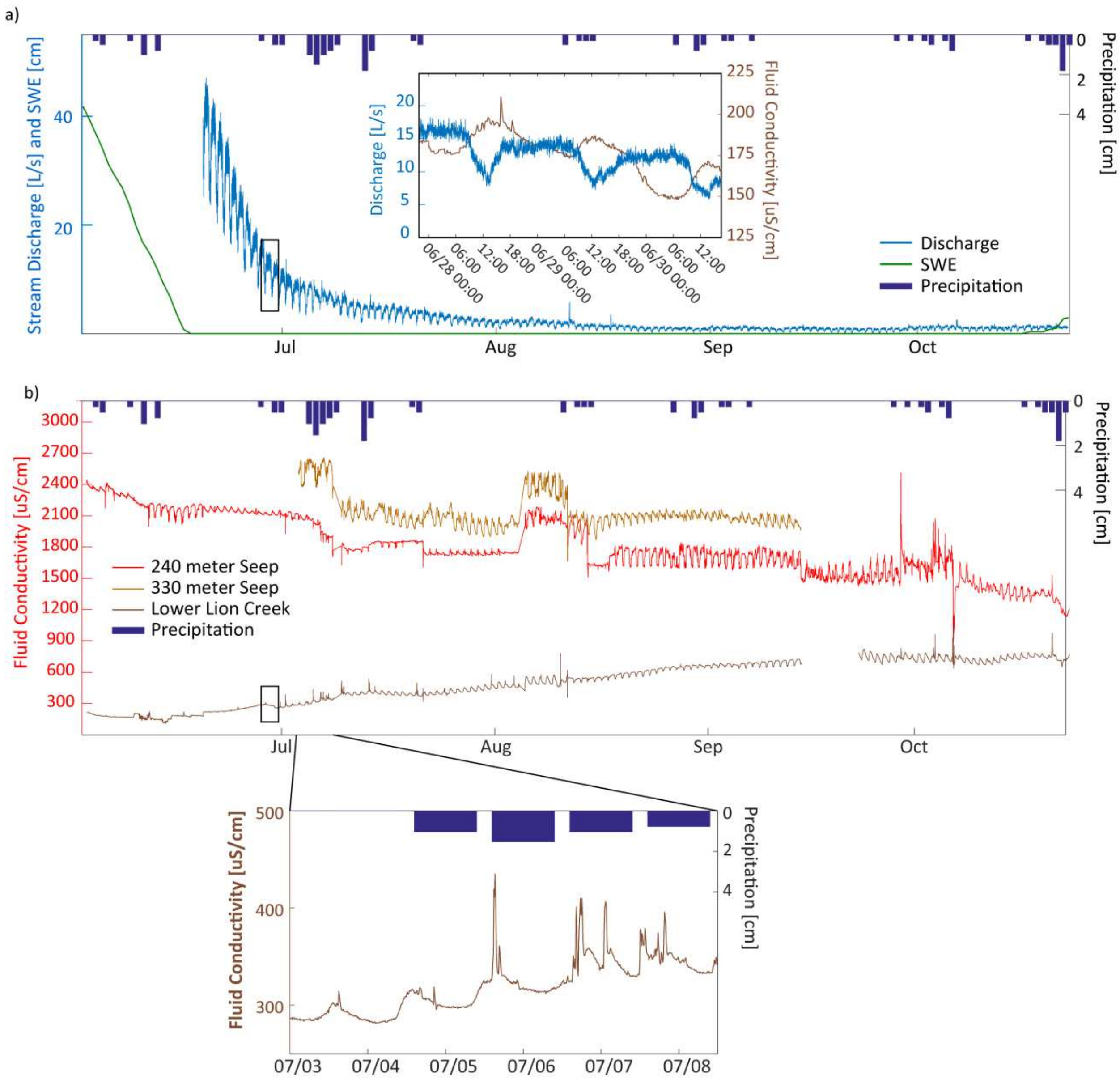

Figure 2.3: (a) Snow water equivalent depth at the Berthoud Summit SNOTEL site, precipitation and Lion Creek discharge. The inset in the middle of the plot shows discharge and σ_f over two and a half days so that the diel cycle is apparent. (b) The time series σ_f of Lion Creek, the 240-m seep and the 330-m seep.

Stream σ_f decreases during the first two weeks of June when the logger was initially deployed (Figure 2.3b), likely because of large amounts of freshwater input from snowmelt based on a rapid decrease in SWE values during the same time period (Figure 2.3a). As the SWE values trend toward zero and discharge rapidly decreases, the stream σ_f then begins to increase. The stream σ_f increases from the middle of June until roughly the end of September, likely because of steadily decreasing inputs of freshwater. Stream σ_f reaches a steady level at the end of September, indicating that attenuation mechanisms are balancing the TDS input to the stream. The average daily stream σ_f increases by 250% between 3 June 2015 and 22 October, 2015. During this same time period, the average daily σ_f of the seep water decreases by 50% (Figure 2.3b). This suggests that different processes affect the concentration of dissolved species in the seep water than in the stream water over the study period.

The decrease in seep σ_f follows the pattern reported by many first flush studies (e.g., Brooks et al. 2001; August et al. 2002) in which constituent concentrations increase during the rising limb of the stream hydrograph and decrease during the falling limb. Decreasing σ_f was also observed in monitoring wells at an AMD-impacted study reach 20 km to the southwest of our site in Bethune et al. (2015) from July to October as stream discharge was declining. Dissolved constituents in the seep water are not affected by snowmelt dilution as strongly as the dissolved constituents in the stream water, which is volumetrically dominated by snowmelt.

The stream σ_f also increases as a result of precipitation. This is counter to the dilution effect, but has been observed in numerous other studies and is attributed to runoff washing metals that have been deposited on the streambank by high flows back into the stream (e.g., Olías et al. 2004; Sarmiento et al. 2009; Nordstrom 2011). At this site, metal salts are visible on the stream bank in the area where tailings are present, and in the large eroded area surround the 240-m seep. Rainfall runoff washing over these areas is likely to dissolve and mobilize additional metals, causing the spikes in stream σ_f seen in the data. However, precipitation does not cause spikes in seep σ_f as it does for stream σ_f. It appears that in many instances where stream σ_f spikes upward due to precipitation, seep σ_f spikes downward. This indicates that precipitation dilutes the concentration of dissolved constituents in the seepages along the stream, even as it washes more dissolved constituents into the stream. This phenomena can be seen most clearly in response to precipitation in July, shown in Figure 2.3b.

In this study, the temporal resolution of the individual species concentration data is too coarse to develop concentration-discharge relationships for each constituent. Because of this, we explore the stream σ_f at Lower Lion Creek versus the discharge measured hourly at the upper stilling well from 19 June 2015 to 23 October 2015 (Figure 2.4). If the relationship between σ_f and TDS is linear, the line indicating perfect dilution of dissolved solids would have a slope of -1 on the log-log axis. This is shown in Figure 2.4 by the blue arrow. While not shown in Figure 2.4, the diel cycles in discharge and σ_f cause higher discharge and lower σ_f at night, meaning the data points shift downward and to the right from day to night. Many of the data points that fall above and to the right of the linear trend are from days with precipitation. This is the result of the event-based increases in σ_f and slight increases in discharge due to precipitation.

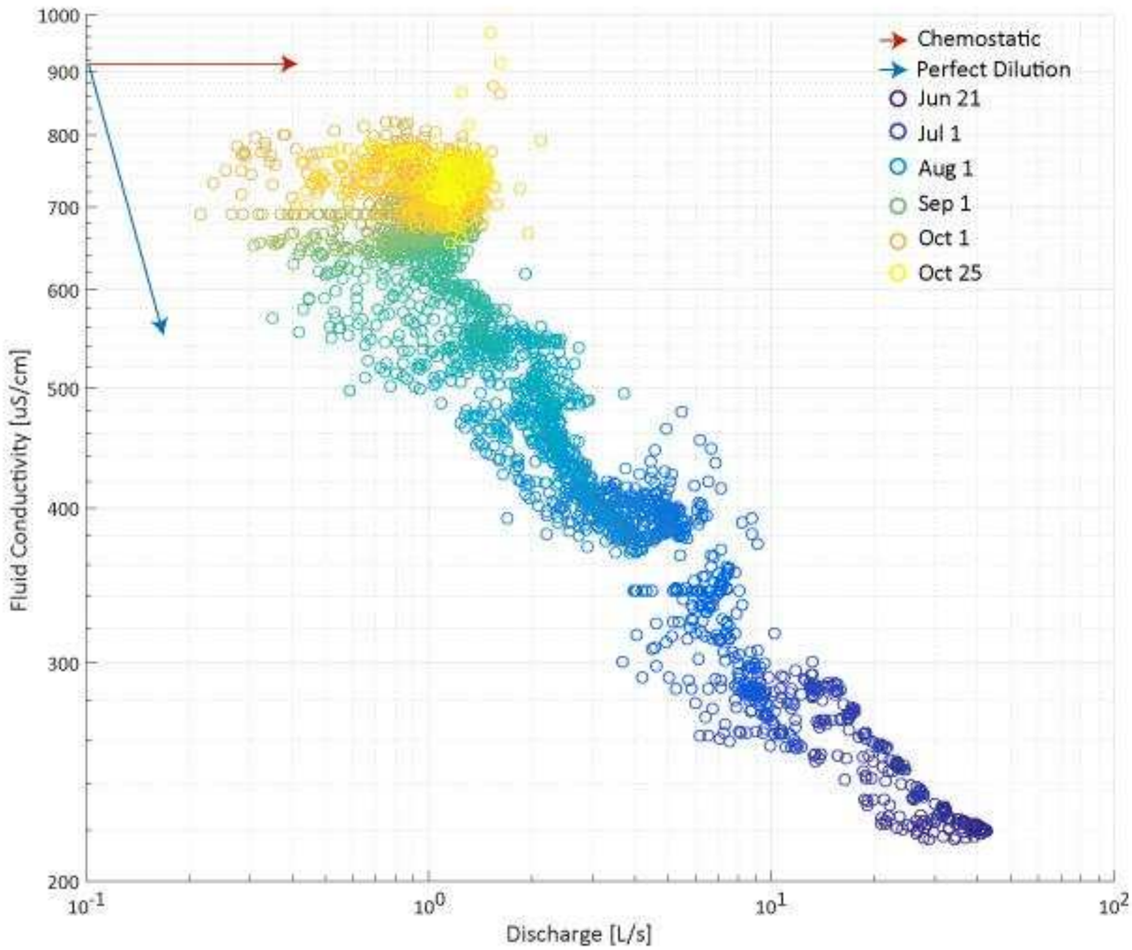

Figure 2.4: Fluid conductivity versus discharge at the upper stilling well from 19 June to 23 October 2015. The data points are hourly averages of σ_f and discharge data.

The equation that best describes the data shown in Figure 2.4 is

$$\sigma_f = 1585 * Q^{-0.32} \qquad (2.19)$$

where σ_f is in µS/cm and Q is discharge in L/s. The exponent -0.32 in equations 2.19 indicates that the relationship between σ_f and discharge is in between chemostatic (exponent of 0) and dilution (exponent of -1) (Godsey et al. 2009). We hypothesize that dilution portion of this system is due to the input of relatively fresh water from snowmelt because the effect of precipitation is counter to the dilution effect, and stream discharge does not appear to be very sensitive to precipitation events (Figure 2.3a).

Additionally, inputs from groundwater not impacted by the mine, likely upstream of the study reach, can dilute concentrations of AMD constituents. One element of the chemostatic portion of this system is likely higher flows entraining metal-rich sediments and therefore increasing σ_f (e.g., Nordstrom 2011). Also, groundwater impacted by AMD could be entering the stream; Runkel (personal communication, 2016) did a tracer test in the same reach of Lion Creek as this study, and found that the stream is gaining throughout the reach, even upstream of the surface seep input. Additionally, preliminary EPA investigations into the site suggest groundwater is mine-impacted in many monitoring wells in the Clear Creek/Central City Superfund site, especially in the alluvial aquifers near mine waste (Looby 1991).

In this study, the temporal resolution of the individual species concentration data is too coarse to develop meaningful loading profiles for each constituent. Because of this, we explore the stream TDS at Lower Lion Creek versus the discharge measured hourly at the upper stilling well from 19 June, 2015 to 23 October, 2015 (Figure 2.4). First, the calculated stream TDS based on σ_f (Equation 2.17) was compared to the TDS of the water samples, calculated by summing the concentration of each constituent measured. The measured TDS is similar to the calculated TDS on each water sample date. This confirms that the empirical relationship between σ_f and TDS is valid at this field site.

Table 2.1: Measured and calculated TDS.

	8-Jul	**4-Aug**	**14-Aug**
TDS, measured [mg/L]	303	427	573
TDS, calculated	317	473	542

The stream TDS was used to calculate a TDS load over the field season. The load is highest in the early summer when discharge is high and stream TDS is relatively low. The load decreases to its lowest levels in September and then climbs slightly in October as discharge increases slightly. There is a strong diel signal in the TDS load due to the strong diel signal in discharge. Quantifying the TDS load is important for informing remediation decisions.

2.5.3 EMI

EMI was used to survey the large open field south of the mine outlet (Figure 2.1). There is an area with significantly higher σ_b than the rest of the field according to the EMI (Figure 2.5a). This conductive area could be indicative of a region in which the shallow groundwater is contaminated by high conductivity AMD, or it could simply be a product of the erosion control work that was done in 1996. Three ERI transects were run through the area to investigate the subsurface structure of the area (Figures 2.5b –d).

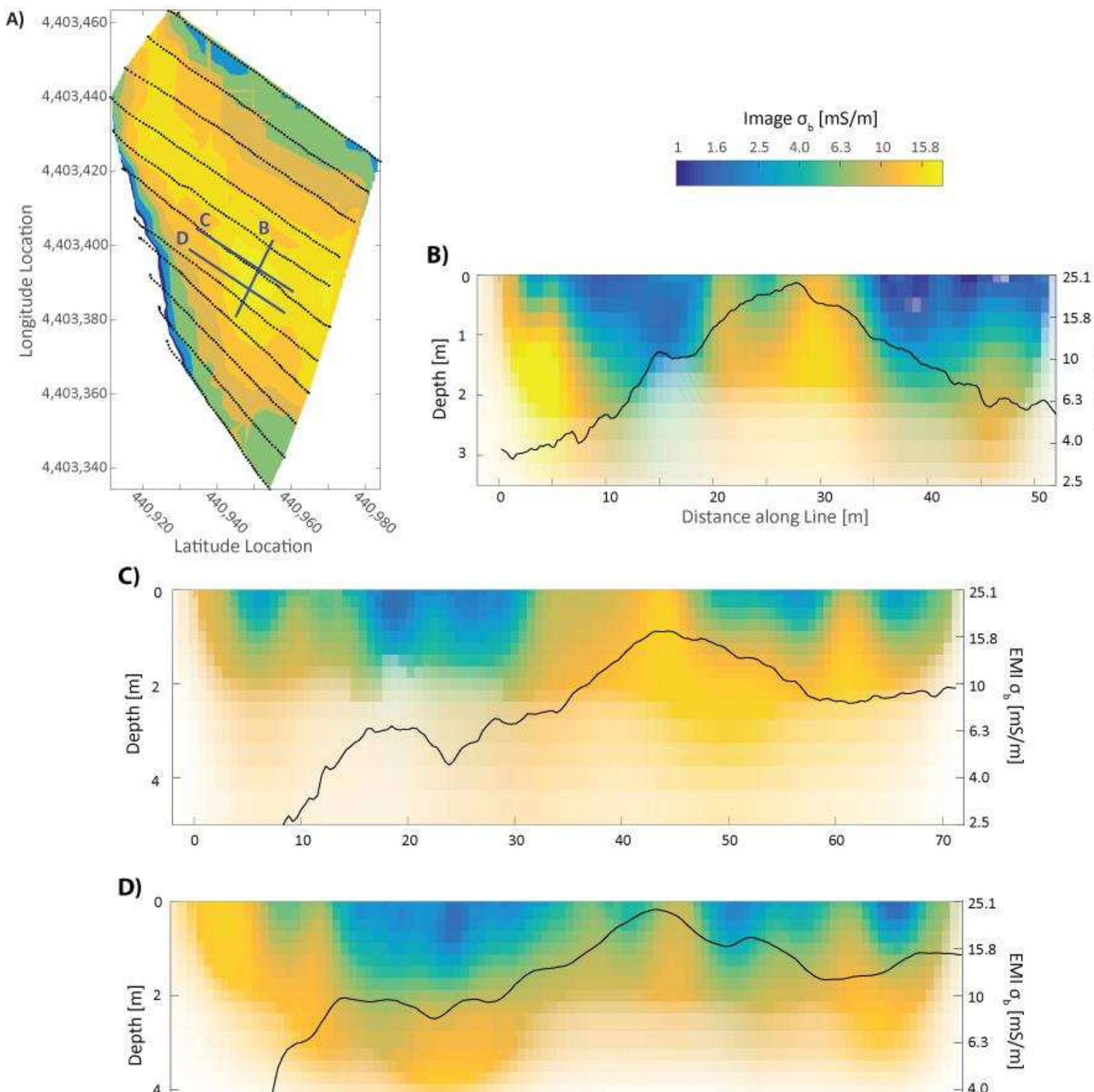

Figure 2.5: (a) EMI data collected on 16 July 2015 on the remediated field south of the mine outlet. The black dots show the locations of the conductivity measurements that were used to create the image using linear triangular interpolation and the blue lines indicate the location of the ERI transects (b-d) ERI images with EMI σ_b plotted on top for comparison.

These Figures 2.5b-d show that the EM31 σ_b correlates well to the σ_b map the ERI produced, although EM31 conductivity is an average of the first 6 m of the subsurface. The ERI maps show a low σ_b layer on the surface underlain by a high σ_b layer. It appears that the high σ_b layer reaches the surface where the EM31 image shows the conductive area. It is not possible to determine whether the conductive layer is connected to the mine or stream using this data set. While there is water quality evidence linking the mine to the stream, the mine water must be traveling through the subsurface at depths greater than what the EMI or ERI can investigate; the elevation change between the opening to the mine adit and the stream was 11 m at its minimum, which is deeper than either method can see in the setup used.

2.5.4 ERI

Replicate ERI data sets were collected between May and October along the study reach. A single ERI image from 23 June is presented in Figure 2.6 because the temporal trends in σ_b are small; the average apparent σ_b was between 7.4 and 8.0 mS/m for each data set through time. An analysis of variance (ANOVA) test done to test the hypothesis that the mean of each of the apparent σ_b distribution is the same confirmed that to a confidence level of >99%, the distributions share the same mean. Only the upper and lower ends of the study reach notably increase in inverted σ_b throughout the study period. The σ_b in this section increases by about 10% in the 2 October dataset compared to 12 May levels, indicating that the process that raises the σ_b in the section intensifies slightly at the end of summer and start of fall. The inversion done to produce the image shown in Figure 2.6 used a homogeneous halfspace of 10 mS/m as a reference model, since replicate ERI datasets are not presented.

The DOI index was calculated for each box in the inverted σ_b model, and the results are presented in Figure 2.6 as black contour lines. The image was made increasingly transparent once the DOI index becomes greater than 0.4. The 0.4 DOI contour is near or at the surface in the interval from 80 to 160 m along the study reach. In this section of the transect it was difficult to minimize the contact resistance between the electrodes, resulting in larger stacking errors and thus measurements that were de-weighted in the inversion scheme. The model has a very deep 0.4 DOI contour from 205 m to 240 m along the study reach, indicating that current was conducted deeper into the subsurface in that section so that the ERI measurements are more sensitive with depth. In this way, σ_b is the main control of the depth of investigation of the ERI measurements.

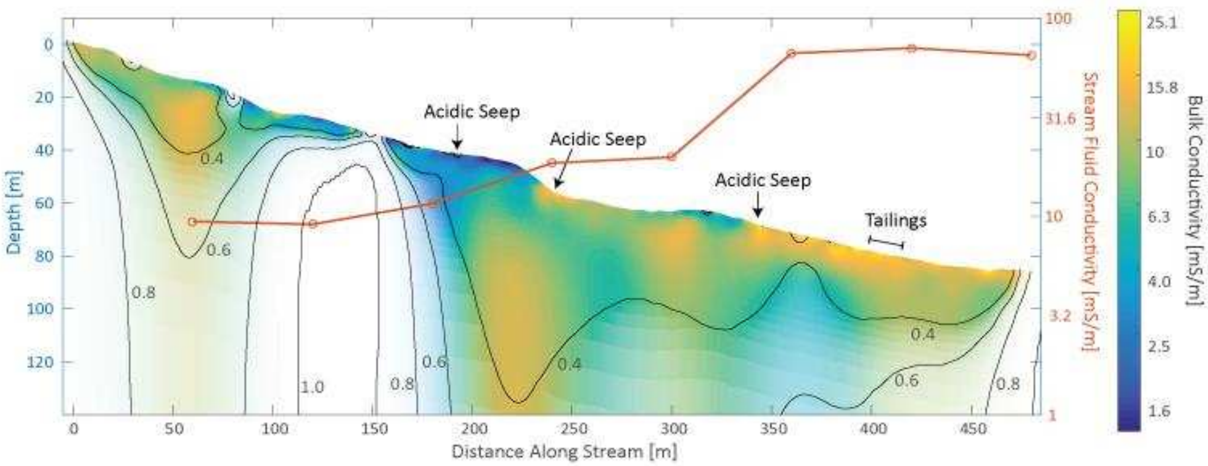

Figure 2.6: ERI data set from 23 June 2015 with the average stream σ_f measured with the handheld probe. The black contour lines indicate the DOI index. The ERI data with a DOI index greater than 0.4 is increasingly transparent. Field observations of seeps and tailings are labeled on the image as well.

The ERI map shows elevated σ_b in the area of the 240-m and 330-m seeps, but not in the vicinity of the 180-m seep. We suspect that the difference here is because of the higher pH and lower total iron content than the other seeps, which indicates a lower σ_f and resultant lower σ_b. Also, there is a thick layer of moss growing in the seep which could deposit organic matter that reduces σ_b as well. The σ_b data generally match with increases in stream σ_f, the orange line in Figure 2.6. At about 315 m, the stream σ_f increases notably; at this location there is a layer with low σ_b at the surface underlain by a layer with higher σ_b. We hypothesize that the conductive area in the subsurface from about 290 to 320 m along the study reach is a subsurface continuation of the seeps visible on surface at 240 and 330 m along the study reach. The location coincides with the jump in σ_f of the stream (Figure 2.6), so it is likely the high σ_f, acidic water is entering the hyporheic zone and slowly mixing with the stream water over this section of the study reach. From about 360 m to the end of the study reach, the temporally averaged stream σ_f is nearly constant. This suggests that the dissolved constituents entering the stream are balanced by the dissolved species leaving the stream via precipitation or other biogeochemical attenuation processes.

The subsurface beneath the tailings piles from 390 m to 410 m in Figure 2.6 is more conductive than the area around it. Due to the presence of the tailings pile, we hypothesize that when water infiltrates through the tailings pile, it leaches metal from the tailings. This high σ_f water then infiltrates into the subsurface, which is a likely cause of the high σ_b seen in the ERI image. The high σ_f water likely mixes with stream water in the hyporheic zone, making the tailings pile leachate a diffuse contamination source to the stream.

There are two other notable high σ_b areas visible in Figure 2.6. One is located from about 40 to 55 m along the study reach. Another is located between 205 and 245 m along the study reach beneath a layer of lower σ_b material. This anomaly is notable because the measurement sensitivity with depth is increased to about 80 m below the ground surface, indicating that the porous media conducted current to depths much greater here than elsewhere along the study reach. It is important to note that σ_b is sensitive to lithology as well, so not every high σ_b area is necessarily the result of acidic, high TDS AMD water. The increase in σ_b could be caused by higher permeability material, or higher clay content among other things. The shape of the anomaly at 205 to 245 m suggests a conductive fracture, which is likely due to high degree of fracturing and alteration in area. However, it is difficult to know with certainty without more geologic information.

Numerous biogeochemical processes attenuate dissolved metal concentrations and acidity in a stream, such as iron oxidation and precipitation, and metal coprecipitation with the iron oxides. Although there is visible evidence of iron oxidation and precipitation, the σ_f increases and pH decreases down the study reach, indicating the presence of contaminant sources along the study reach, examples of which are seen in surface seeps. The appearance of orange iron hydroxide precipitates upstream of discrete acidic seepage faces as well as the increase in stream σ_f in between the 240-m and 330-m surface seepages indicate that diffuse sources play an important role in the overall contaminant load entering the stream.

2.6 Conclusions

This study leverages electrical conductivity data in addition to the water sampling to investigate a headwater mountain stream affected by AMD. The goals of our study were to identify diffuse and discrete contamination sources and to elucidate seasonal trends in water quality to help inform remediation efforts. A range of field data suggests that there are diffuse sources of AMD affecting Lion Creek. First, there is visible iron precipitate on the streambed upstream of the identified discrete contamination entering the stream from visible seepage faces. Second, the average stream σ_f increased in between the 240-m seep and 330-m seep discrete sources. The ERI map shows areas of elevated σ_b in the subsurface beneath the 240-m seep and 330-m seep as well as between the two seeps. Because of this, we hypothesize that the two seeps have a subsurface portion as well that is contributing AMD-impacted water to the stream. Additionally, the ERI map shows a conductive area beneath the tailings pile at 390 to 410 m. This is likely due to acidic, high TDS leachate from the tailings infiltrating into the subsurface. Some of this water likely enters the hyporheic zone and then stream due to the proximity of the tailings to the stream. This is another likely source of diffuse contamination. The identification of diffuse contamination sources allows for more spatially targeted remediation options, such as removing the tailings beside Lion Creek and installing a permeable reactive barrier along the east bank of the stream from about 230 to 340 m that could intercept discrete and diffuse contamination entering the stream in that reach. Of course, σ_b is sensitive to lithology as well as σ_f; consequently, these data should be considered a way of focusing new sampling in areas that might not have been previously considered.

Seasonal variation in water quality was investigated using a range of field data. The period of record for σ_f and discharge data in this study was from June to October, or from the falling limb of the stream hydrograph to the later summer baseflow. The results of this study indicate that the TDS load is highest during early summer, when discharge is highest. There is a large diel variation in the TDS load, likely due to the large diel fluctuation in stream discharge. This information may be helpful for estimating the cost of different remediation scenarios and potentially for determining a maintenance schedule for things like sludge removal in the case of a settling pond by helping planners estimate the volume and timing of sludge generation. The results of this study also indicate that seasonal variation in stream σ_f is largely dilution controlled, with snowmelt being the largest contributor of fresh water. The exception is following precipitation events, when there is an increase in σ_f resulting from rainfall runoff washing soluble metal salts deposited on the stream bank back into the stream. This is another source of diffuse contamination. Although stream σ_f increases throughout the field season by 250%, seep σ_f decreases by 50%. Many previous studies have reported falling pore water σ_f during the falling limb of the stream hydrograph after an increase due to first flush. Therefore, over the field season we have seep σ_f declining from high first flush levels and stream σ_f increasing due to declining fresh water inputs.

There does not appear to be strong temporal patterns in the replicate ERI or EMI data sets, collected between May and October. However, there is a strong seasonal trend in stream and seep σ_f. One reason seasonal variation is not seen in the ERI σ_b data sets is that in media containing minerals with a high CEC, current can travel along the mineral grain surfaces, increasing the measured σ_b (Equation 2.14). The amount of additional charge depends on the ionic strength of the pore water, with the effect greatest at low ionic strength (Singha et al. 2011). In this way, surface conductance obscures the direct relationship between σ_f and σ_b in saturated media, and could be masking the effects of decreasing pore σ_f over the field season. Additionally, the σ_b values in the inverted ERI image are volume averages over the model grid cell. Due to the averaging and the regularization done in the inversion process, anomalies need to be large in magnitude and spatial extent in order to be visible. Bethune et al. (2015) showed that low σ_b anomalies with radii of less than 4 m may go undetected in the inverted image, especially if they are deep. Though the spatial extent and magnitude required for anomalies to be visible in the inverted image varies between sites, it is possible that there are anomalies in this data set that just are not spatially large enough or of a low enough σ_b to be visible post inversion.

The goal we had for the EMI data set was to delineate flow paths of AMD water from the mine to the stream. However, the EMI data in the remediated field does not have a deep enough depth of investigation to show increases in σ_b that can be related to subsurface flow paths of AMD water. The steep topography and rough terrain of the area between the mine and stream outside of the remediated field did not allow for valid EMI measurements because the instrument is very sensitive to its position relative to the ground. Other geophysical methods, including EMI using the EM34, which allows the user to control the instrument intercoil spacing and therefore the depth of investigation, would be applicable in the remediated field. Bethune et al. (2015) demonstrated the utility of time lapse geophysical methods in AMD site characterization, however this data set was not able to overcome confounding factors in the σ_f to σ_b relationship and depth of investigation shortcomings.

Measuring σ_f and σ_b is a low cost method to determine the relative level of AMD contribution to a stream. The collection of σ_b data in the shallow subsurface yielded important information about the spatial distribution of potential diffuse contamination entering the stream, and provides a guideline for future sampling locations. Additionally, σ_f logging was valuable as a low-cost way to collect information about the general level of contamination in the stream and seeps throughout the field season. Although geochemical samples yield more detailed water quality information, it would be impractical to get the same temporal resolution of water quality information using geochemical samples.

CHAPTER 3

FUTURE WORK

Though we were successful in identifying likely diffuse contamination sources and qualifying seasonal variation in AMD contribution levels, there are still many persistent questions: what are the explicit flow paths of AMD water from the mine to the stream? Can the diffuse contamination sources be confirmed? Can we quantify seasonal variation in individual constituent loads? Is the variation the same year after year? What are the site specific controls on seasonal variation? Finally, can we expect similar results at different mine-stream systems in the area?

The conductive area in the remediated field warrants furthers study. First, soil cores from the place where the conductive layer reaches the surface could be compared to soil cores from elsewhere in the field. This would help determine if the change in σ_b is due to differing soil material or elevated σ_f pore water. If the change is due to elevated σ_f pore water, AMD flow paths could potentially be delimited by measuring σ_b in the remediated field between the mine and the stream to deeper depths. Some potentially useful geophysical methods for this include (1) EM34, an EMI tool which allows the intercoil spacing, and therefore the DOI, to be controlled by the user, and sees deeper than the EM31 or (2) ERI with a larger electrode spacing and borehole electrodes to increase the measurement sensitivity at depth (e.g., Binley and Kemna 2005; Rucker et al. 2009a). Unfortunately, the steep topography of the streambank as well as the continuing erosion outside of the remediated area preclude us from gathering geophysical data outside of the remediated field and the area in the immediate vicinity of the stream. The diffuse contamination sources could be confirmed by installing piezometers in the areas along the stream that are suspected to contribute diffuse contamination.

The stream in the draw to the east of Lion Creek, called Empire Creek, is suspected to be receiving AMD from the Conqueror Mines. A replicate study along Empire Creek could show whether the diel and seasonal patterns in σ_f are similar between the two mine-stream systems. If a similar diel and seasonal pattern of σ_f are seen in Empire Creek and any surface seeps affecting the Empire Creek, it may be possible to generalize about mine-stream systems in the area with similar geology. Also, Runkel (personal communication 2016) found that the North Empire Creek inflow (Figure 2.1) contributes a significant portion of the AMD constituent load to Lion Creek. This study could be expanded to include the entire Lion Creek watershed.

An event-based increase in stream σ_f was observed during precipitation events. This could have a major impact on water quality and is an area that needs more study. Water samples taken during and shortly after precipitation events could indicate whether the increase in stream σ_f is made up of additional dissolved solids that are of water quality concern.

Like most inactive mine site investigations, this study is limited by the amount of information available about the site. Lion Creek has not been studied as extensively as other mine-impacted rivers and streams in the Colorado Mineral Belt. This study, as well as the concurrent study done by Runkel, will help inform USFS remediation effort; however, there is still opportunity for further study. Banks and Palumbo-Roe (2010) suggest that AMD site investigation is an iterative process, in which hypotheses from previous studies are tested in subsequent studies. This certainly applies at Minnesota Mine; subsequent studies could direct their attention to the areas we hypothesized are diffuse contamination sources impacting Lion Creek.

REFERENCES CITED

Akcil A, Koldas S (2006) Acid Mine Drainage (AMD): causes, treatment and case studies. J Clean Prod 14:1139–1145. doi: 10.1016/j.jclepro.2004.09.006

Archie GE (1942) The Electrical Resistivity Log as an Aid in Determining Some Reservoir Characteristics. Pet Technol 54–62. doi: 10.2118/942054-G

August EE, McKnight DM, Hrncir DC, Garhart KS (2002) Seasonal variability of metals transport through a wetland impacted by mine drainage in the Rocky Mountains. Environ Sci Technol 36:3779–3786. doi: 10.1021/es015629w

Banks D, Younger PL, Arnesen R-T, et al (1997) Mine-water chemistry: The good, the bad and the ugly. Environ Geol 32:157–174. doi: 10.1007/s002540050204

Banks VJ, Palumbo-Roe B (2010) Synoptic monitoring as an approach to discriminating between point and diffuse source contributions to zinc loads in mining impacted catchments. J Environ Monit 12:1684–98. doi: 10.1039/c0em00045k

Baresel C, Destouni G, Gren IM (2006) The influence of metal source uncertainty on cost-effective allocation of mine water pollution abatement in catchments. J Environ Manage 78:138–148. doi: 10.1016/j.jenvman.2005.03.013

Baron JS, Campbell DH (1997) Nitrogen fluxes in a high elevation Rocky Mountain basin. Hydrol Process 11:783–799. doi: 10.1002/(SICI)1099-1085(199706)11:7<783::AID-HYP519>3.3.CO;2-L

Bencala KE, Walters RA (1983) Simulation of solute transport in a mountain pool-and-riffle stream: A transient storage model. Water Resour Res 19:718. doi: 10.1029/WR019i003p00718

Benson AK, Addams CL (1998) Detecting the presence of acid mine drainage using hydrogeological, geochemical, and geophysical data: application to contrasting conditions at mine sites in Little Cottonwood and American Fork Canyons, Utah. Environ Geosci 5:17–27. doi: 1075-9565

Bethke CM, Yeakel S (2015) GWB- Essentials Guide. Geochemist's Work. Release 10.0 116.

Bethune J, Randell J, Runkel RL, Singha K (2015) Non-invasive flow path characterization in a mining-impacted wetland. J Contam Hydrol 183:29–39. doi: 10.1016/j.jconhyd.2015.10.002

Binley A, Kemna A (2005) DC Resistivity and Induced Polarization Methods. Hydrogeophysics 50:129–156. doi: 10.1007/1-4020-3102-5

Boyer EW, Hornberger GM, Bencala KE, Mcknight DM (1997) Response Characteristics of Doc Flushing in an Alpine Catchment. Hydrol Process 11:1635–1647. doi: 10.1002/(SICI)1099-1085(19971015)11

Braddock WA (1969) Geology of the Empire Quadrangle Grand, Gilpin, and Clear Creek Counties Colorado.

Brooks PD, McKnight DM, Bencala KE (2001) Annual maxima in Zn concentrations during spring snowmelt in streams impacted by mine drainage. Environ Geol 40:1447–1454. doi: 10.1007/s002540100338

Buselli G, Hwang HS, Lu K (1998) Minesite groundwater contamination mapping. Explor Geophys 29:296. doi: 10.1071/EG998296

Buselli G, Lu K (2001) Groundwater contamination monitoring with multichannel electrical and electromagnetic methods. J Appl Geophys 48:11–23. doi: 10.1016/S0926-9851(01)00055-6

Butler B, Ranville J, Ross P (2009) Spatial variations in the fate and transport of metals in a mining-influenced stream, North Fork Clear Creek, Colorado. Sci Total Environ 407:6223–6234. doi: 10.1016/j.scitotenv.2009.08.040

Butler B, Ranville J, Ross P (2008) Observed and modeled seasonal trends in dissolved and particulate Cu, Fe, Mn, and Zn in a mining-impacted stream. Water Res 42:3135–3145. doi: 10.1016/j.watres.2008.03.004

Caruso BS, Cox TJ, Runkel RL, et al (2008) Metals fate and transport modelling in streams and watersheds: state of the science and USEPA workshop review. Hydrol Process 22:4011–4021. doi: 10.1002/hyp.7114

Cassiani G, Bruno V, Villa A, et al (2006) A saline trace test monitored via time-lapse surface electrical resistivity tomography. J Appl Geophys 59:244–259. doi: 10.1016/j.jappgeo.2005.10.007

Chandra a. P, Gerson a. R (2010) The mechanisms of pyrite oxidation and leaching: A fundamental perspective. Surf Sci Rep 65:293–315. doi: 10.1016/j.surfrep.2010.08.003

Cunningham CG, Naeser CW, Marvin RF, et al (1994) Ages of Selected Intrusive Rocks ana Associated Ore Deposits in the Colorado Mineral Belt. US Geol Surv Bull 2109:1–37.

Day-Lewis FD, Singha K, Binley AM (2005) Applying petrophysical models to radar travel time and electrical resistivity tomograms: Resolution-dependent limitations. J Geophys Res B Solid Earth 110:1–17. doi: 10.1029/2004JB003569

deGroot-Hedlin C (1990) Occam’s inversion to generate smooth, two-dimensional models from magnetotelluric data. Geophysics 55:1613. doi: 10.1190/1.1442813

DeNicola DM, Stapleton MG (2002) Impact of acid mine drainage on benthic communities in streams: The relative roles of substratum vs. aqueous effects. Environ Pollut 119:303–315. doi: 10.1016/S0269-7491(02)00106-9

Dodson MH (2004) Five-Year Review Report for Clear Creek/Central City Superfund Site Gilpin and Clear Creek Counties. Denver, CO

Ebraheem AM, Hamburger MW, Bayless ER, Krothe NC (1990) Study of acid mine drainage using earth resistivity measurements. Ground Water 28:361–368.

Elder K, Dozier J, Michaelsen J (1991) Snow accumulation and distribution in an Alpine Watershed. Water Resour Res 27:1541–1552. doi: 10.1029/91WR00506

Evangelou VP (Bill), Zhang YL (1995) A review: Pyrite oxidation mechanisms and acid mine drainage prevention. Crit Rev Environ Sci Technol 25:141–199. doi: 10.1080/10643389509388477

Godsey SE, Kirchner JW, Clow DW (2009) Concentration-discharge relationships reflect chemostatic characteristics of US catchments. Hydrol Process 23:1844–1864. doi: 10.1002/hyp.7315

Gozzard E, Mayes WM, Potter HAB, Jarvis AP (2011) Seasonal and spatial variation of diffuse (non-point) source zinc pollution in a historically metal mined river catchment , UK. Environ Pollut 159:3113–3122. doi: 10.1016/j.envpol.2011.02.010

Hall FR (1970) Dissolved Solids-Discharge Relationships: 1. Mixing Models. Water Resour Res 6:845–850. doi: 10.1029/WR006i003p00845

Hall FR (1971) Dissolved Solids-Discharge Relationships: 2. Applications to Field Data. Water Resour Res 7:591–601. doi: 10.1029/WR007i003p00591

Hallberg KB (2010) New perspectives in acid mine drainage microbiology. Hydrometallurgy 104:448–453. doi: 10.1016/j.hydromet.2009.12.013

Hayashi M (2004) Temperature-electrical conductivity relation of water for environmental monitoring and geophysical data inversion. Environ Monit Assess 96:119–128. doi: 10.1023/B:EMAS.0000031719.83065.68

Hazen JM, Williams MW, Stover B, Wireman M (2002) Characterisation of acid mine drainage using a combination of hydrometric, chemical and isotopic analyses, Mary Murphy Mine, Colorado. Environ Geochem Health 24:1–22. doi: 10.1023/A:1013956700322

Herbert RB (2006) Seasonal variations in the composition of mine drainage-contaminated groundwater in Dalarna, Sweden. J Geochemical Explor 90:197–214. doi: 10.1016/j.gexplo.2005.12.002

Hornberger GM, Bencala KE, McKnight DM (1994) Hydrological controls on dissolved organic carbon during snowmelt in the Snake River near Montezuma, Colorado. Biogeochemistry 25:147–165. doi: 10.1007/BF00024390

Johnson DB, Hallberg KB (2005) Acid mine drainage remediation options: A review. Sci Total Environ 338:3–14. doi: 10.1016/j.scitotenv.2004.09.002

Kemna A, Kulessa B, Vereecken H (2002) Imaging and characterisation of subsurface solute transport using electrical resistivity tomography (ERT) and equivalent transport models. J Hydrol 267:125–146. doi: 10.1016/S0022-1694(02)00145-2

Kimball BA, Church SE, Besser JM (2006) Lessons learned from the U.S. Geological Survey abandoned mine lands initiative - 1997-2002.

Kimball BA, Runkel RL, Walton-Day K (2010) An approach to quantify sources, seasonal change, and biogeochemical processes affecting metal loading in streams: Facilitating decisions for remediation of mine drainage. Appl Geochemistry 25:728–740. doi: 10.1016/j.apgeochem.2010.02.005

Kimball BA, Runkel RL, Walton-Day K, Bencala KE (2002) Assessment of metal loads in watersheds affected by acid mine drainage by using tracer injection and synoptic sampling: Cement Creek, Colorado, USA. Appl Geochemistry 17:1183–1207. doi: 10.1016/S0883-2927(02)00017-3

LaBrecque DJ (1996) The effects of noise on Occam's inversion of resistivity tomography data. Geophysics 61:538. doi: 10.1190/1.1443980

LaBrecque DJ, Yang X (2001) Difference inversion of ERT data: a fast inversion method for 3-D in situ monitoring. J Environ Eng Geophys 6:83–89. doi: 10.4133/JEEG6.2.83

Ladwig KJ (1983) Electromagnetic induction methods for monitoring acid mine drainage. Gr Water Monit Rev 3:46–51.

Loke MH, Chambers JE, Rucker DF, et al (2013) Recent developments in the direct-current geoelectrical imaging method. J Appl Geophys 95:135–156. doi: 10.1016/j.jappgeo.2013.02.017

Looby TB (1991) EPA Superfund Record of Decision: Central City, Clear Creek EPA ID: MOD006333975.

Lovering TS, Goddard EN (1950) Geology and Ore Deposits of the Front Range Colorado. 2:333 pp.

Luther GW (1987) Pyrite oxidation and reduction: Molecular orbital theory considerations. Geochim Cosmochim Acta 51:3193–3199. doi: 10.1016/0016-7037(87)90127-X

Malan H, Bath A, Day J, Joubert A (2004) A simple flow-concentration modelling method for integrating water quality and water quantity in rivers. Water SA 29:305–312. doi: 10.4314/wsa.v29i3.4932

Martín-Crespo T, Martín-Velázquez S, Gómez-Ortiz D, et al (2011) A geochemical and geophysical characterization of sulfide mine ponds at the Iberian Pyrite Belt (Spain). Water Air Soil Pollut 217:387–405. doi: 10.1007/s11270-010-0595-6

McDiffett WF, Beidler AW, Dominick TF, McCrea KD (1989) Nutrient concentration-stream discharge relationships during storm events in a first-order stream. Hydrobiologia 179:97–102. doi: 10.1007/BF00007596

McNeill JD (1980) Electromagnetic Terrain Conductivity Measurement at Low Induction Numbers. Geonics Ltd. Technical :

McNeill JD (1983) Use of EM31 Inphase Information.

Merkel RH (1972) The use of resistivity techniques to delineat acid mine drainage in ground water. Ground Water 10:38–42.

Mighanetara K, Braungardt CB, Rieuwerts JS, Azizi F (2009) Contaminant fl uxes from point and diffuse sources from abandoned mines in the River Tamar catchment , UK. J Geochemical Explor 100:116–124. doi: 10.1016/j.gexplo.2008.03.003

Moses C, Herman J (1989) Homogeneous oxidation kinetics of aqueous ferrous iron at circumneutral pH. J Solution Chem 18:705–725. doi: 10.1007/BF00651804

Moses C, Herman JS (1991) Pyrite oxidation at circumneutral pH. Geochim Cosmochim Acta 55:471–482. doi: 91

Moses CO, Kirk Nordstrom D, Herman JS, Mills AL (1987) Aqueous pyrite oxidation by dissolved oxygen and by ferric iron. Geochim Cosmochim Acta 51:1561–1571. doi: 10.1016/0016-7037(87)90337-1

Niyogi DK, Lewis WMJ, McKnight DM (2002) Effects of Stress from mine Draiange on Diversity, Biomass, and Function of Primary Producers in Mountain Streams. Ecosystems 5:554–567.

Nordstrom DK (2009) Acid rock drainage and climate change. J Geochemical Explor 100:97–104. doi: 10.1016/j.gexplo.2008.08.002

Nordstrom DK (2011) Hydrogeochemical processes governing the origin, transport and fate of major and trace elements from mine wastes and mineralized rock to surface waters. Appl Geochemistry 26:1777–1791. doi: 10.1016/j.apgeochem.2011.06.002

Oldenburg DW, Li Y (1999) Estimating depth of investigation in dc resistivity and IP surveys. Geophysics 64:403. doi: 10.1190/1.1444545

Olías M, Nieto JM, Sarmiento a. M, et al (2004) Seasonal water quality variations in a river affected by acid mine drainage: The Odiel River (South West Spain). Sci Total Environ 333:267–281. doi: 10.1016/j.scitotenv.2004.05.012

Radtke DB, Davis J V, Wilde FD (2005) Specific electrical conductance. In: National Field Manual for the Collection of Water-Quality Data (TWRI Book 9). pp 1–22

Ramalho E, Carvalho J, Barbosa S, Monteiro Santos F a. (2009) Using geophysical methods to characterize an abandoned uranium mining site, Portugal. J Appl Geophys 67:14–33. doi: 10.1016/j.jappgeo.2008.08.010

Revil A, Cathles LM, Losh S, Nunn J a. (1998) Electrical conductivity in shaly sands with geophysical applications. J Geophys Res 103:23,925–23,936. doi: 10.1029/98JB02125

Rucker DF, Glaser DR, Osborne T, Maehl WC (2009a) Electrical resistivity characterization of a reclaimed gold Mine to delineate acid rock drainage pathways. Mine Water Environ 28:146–157. doi: 10.1007/s10230-009-0072-x

Rucker DF, Levitt MT, Greenwood WJ (2009b) Three-dimensional electrical resistivity model of a nuclear waste disposal site. J Appl Geophys 69:150–164. doi: 10.1016/j.jappgeo.2009.09.001

Runkel RL (1998) One-dimensional transport with inflow and storage (OTIS): a solute transport model for streams and rivers.

Runkel RL, Kimball B a., Walton-Day K, et al (2012) Evaluating remedial alternatives for an acid mine drainage stream: A model post audit. Environ Sci Technol 46:340–347. doi: 10.1021/es2038504

Runkel RL, Kimball BA (2002) Evaluating Remedial Alternatives for an Acid Mine Drainage Stream: Application of a Reactive Transport Model. 1093–1101.

Runkel RL, Walton-Day K, Kimball B a., et al (2013) Estimating instream constituent loads using replicate synoptic sampling, Peru Creek, Colorado. J Hydrol 489:26–41. doi: 10.1016/j.jhydrol.2013.02.031

Sarmiento AM, Nieto JM, Olías M, Cánovas CR (2009) Hydrochemical characteristics and seasonal influence on the pollution by acid mine drainage in the Odiel river Basin (SW Spain). Appl Geochemistry 24:697–714. doi: 10.1016/j.apgeochem.2008.12.025

Sen PN, Goode PA, Sibbit A (1988) Electrical conduction in clay bearing sandstones at low and high salinities. J Appl Phys 63:4832–4840. doi: 10.1063/1.340476

Sims L, Guerra J (2014) Updated Fact Sheet Central City/Clear Creek Superfund Site.

Singha K, Li L, Day-Lewis FD, Regberg AB (2011) Quantifying solute transport processes: Are chemically “conservative” tracers electrically conservative? Geophysics 76:F53–F63. doi: 10.1190/1.3511356

Smith BBD, Mcdougal RR, Deszcz-pan M, Yager DB (2007) Helicopter Electromagnetic and Magnetic Surveys Mining in the Animas River Watershed , San Juan County , Colorado. Integr Investig Enviornmental Eff Hist Min Animas River Watershed, San Juan County, Color US Geol Surv Prof Pap 1651 235–254.

Smith SH (1962) Temperature correction in conductivity measurements. Limnol Oceanogr 7:330–334. doi: 10.4319/lo.1962.7.3.0330

Taylor BE, Wheeler MC, Nordstrom DK (1984) Stable isotope geochemistry of acid mine drainage: Experimental oxidation of pyrite. Geochim Cosmochim Acta 48:2669–2678. doi: 10.1016/0016-7037(84)90315-6

Tezkan B (1999) A Review Of Environmental Applications Of Quasi-Stationary Electromagnetic Techniques. Surv Geophys 20:279–308. doi: 10.1023/A:1006669218545

Ward AS, Gooseff MN, Fitzgerald M, et al (2014) Spatially distributed characterization of hyporheic solute transport during baseflow recession in a headwater mountain stream using electrical geophysical imaging. J Hydrol 517:362–377. doi: 10.1016/j.jhydrol.2014.05.036

Ward AS, Gooseff MN, Singha K (2010) Imaging hyporheic zone solute transport using electrical resistivity. Hydrol Process 24:948–953. doi: 10.1002/hyp.7672

Waxman MH, Smits LJM (1968) Electrical Conductivities in Oil-Bearing Shaly Sands. Soc. Pet. Eng. Trans. Vol. 243 107–122.

Yuval, Oldenburg DW (1996) DC resistivity and IP methods in acid mine drainage problems: Results from the Copper Cliff mine tailings impoundments. J Appl Geophys 34:187–198. doi: 10.1016/0926-9851(95)00020-8

APPENDIX A: ADDITIONAL DATA AND FIGURES

The figures and tables in this appendix support the results and discussion section in the main text. Figure A1 shows the precipitation and stream σ_f data presented in Figure 2.3 on a smaller scale. It is clear that the spikes in σ_f are well correlated with precipitation events. These transient increases in stream σ_f are significant and may be of importance when making remediation decisions since they are indicative of increased TDS load. Figure A2 below shows metal salts on the streambed. These salts are likely the cause of the σ_f spikes as they wash into the stream with runoff from precipitation.

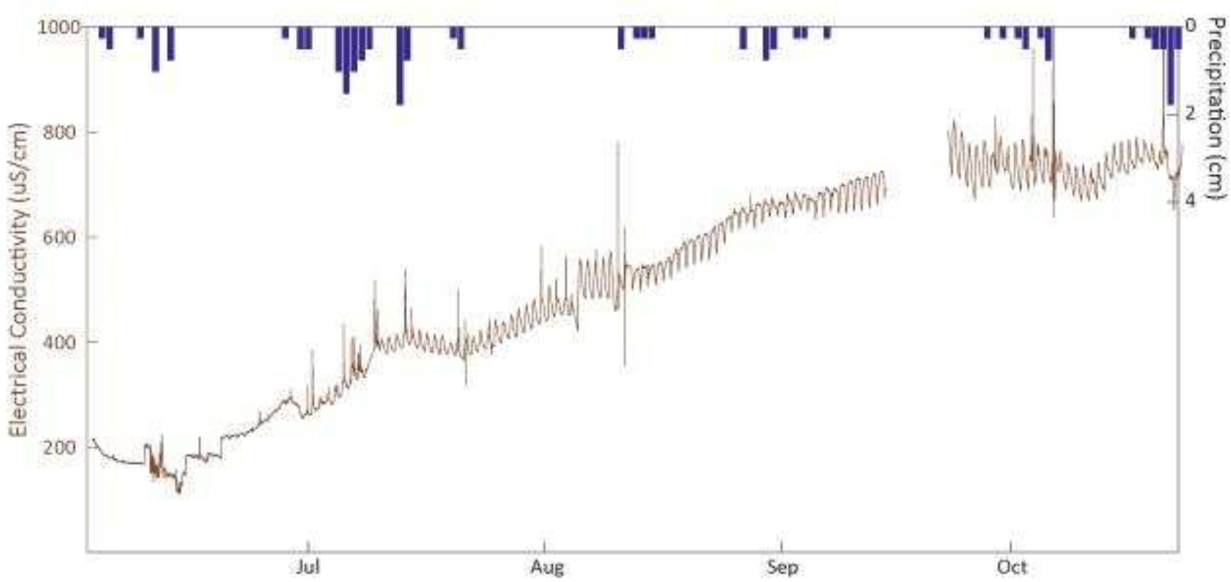

Figure A1: Lower Lion Creek σ_f and precipitation.

Figure A2: Photo from Lion Creek on August 26, 2015 showing metal salts likely to wash back into the stream with runoff from precipitation.

Table A1 shows the complete water sample results from 8 July, 4 August, and 14 August 2015 for the Upper Lion Creek, 180-m seep, and 240-m seep. Table A2 shows the complete water sample results for the 330-m seep and Lower Lion Creek. Trace metals, as well as the typical anions and cations, were tested for. In the table, BDL means below detection level. The pH of the sampled water is also included in the last row of the table. The charge balance of the seepage water samples was 40 to 50%, which indicates an issue with the analysis. The charge balance of each of the samples from Lion Creek was less than 10%, which is acceptable for natural waters.

Table A1: Complete sample results for Upper Lion Creek, 180-m seep and 240-m seep. All concentrations are in mg/L.

	Upper Lion Creek			180-m Seep			240-m Seep		
Species	**8-Jul**	**4-Aug**	**14-Aug**	**8-Jul**	**4-Aug**	**14-Aug**	**8-Jul**	**4-Aug**	**14-Aug**
F	0.12	BDL	0.24	1.44	1.51	1.28	5.08	5.36	5.36
Cl	17.80	BDL	0.73	1.43	3.21	1.25	1.93	3.77	3.77
NO2	BDL	BDL	BDL	BDL	BDL	BDL	BDL	BDL	BDL
Br	BDL	BDL	BDL	BDL	BDL	BDL	BDL	BDL	BDL
NO3	BDL	BDL	BDL	2.24	BDL	BDL	BDL	BDL	BDL
PO4	BDL	BDL	BDL	4.68	BDL	BDL	BDL	BDL	BDL
SO4	5.11	6.07	7.14	597.40	675.37	596.72	1852.6	2050.6	2050.6
O2	5.00	BDL	BDL	3.00	BDL	BDL	3.00	BDL	BDL
Al	0.15	0.02	0.01	27.12	26.96	28.48	58.93	57.49	57.09
As	0.03	BDL	BDL	0.03	BDL	BDL	0.03	BDL	BDL
B	0.24	0.07	0.21	0.32	0.34	0.14	0.31	0.40	0.22
Ba	BDL	0.09	0.11	BDL	0.04	0.07	BDL	0.06	0.08
Be	BDL	BDL	BDL	0.01	0.00	0.00	0.01	0.01	0.01
Ca	3.73	4.29	4.48	47.58	47.42	49.55	114.01	109.73	109.57
Cd	0.04	BDL	BDL	BDL	BDL	BDL	BDL	BDL	BDL
Co	BDL	BDL	BDL	0.11	0.10	0.10	0.33	0.33	0.33
Cr	BDL	BDL	BDL	BDL	BDL	BDL	BDL	0.00	BDL
Cu	0.01	BDL	BDL	0.71	0.65	0.64	1.68	1.57	1.53
Fe	0.05	0.02	0.02	2.79	2.15	2.17	64.93	57.24	57.36
K	17.26	BDL	0.22	2.53	4.58	2.84	0.53	8.12	1.01
Li	BDL	BDL	BDL	BDL	BDL	BDL	BDL	BDL	BDL
Mg	0.80	0.87	0.92	20.29	20.10	20.68	47.19	46.46	45.64
Mn	0.01	BDL	BDL	8.07	7.38	7.28	26.40	26.08	26.10
Na	3.33	3.73	3.79	8.42	8.69	8.83	11.33	11.35	10.97
Ni	BDL	BDL	BDL	0.07	0.06	0.06	0.19	0.19	0.18
P	0.06	BDL	BDL	0.02	BDL	BDL	0.04	0.08	0.04
Pb	BDL	BDL	BDL	BDL	BDL	BDL	BDL	BDL	BDL
S	2.67	3.64	3.69	149.26	150.69	156.62	401.39	399.02	400.22
Se	BDL	BDL	BDL	BDL	BDL	BDL	BDL	BDL	BDL
Si	7.79	7.97	8.04	27.85	26.87	27.79	60.47	62.55	61.26
Sr	BDL	BDL	BDL	0.26	0.26	0.26	0.36	0.35	0.35
Tl	0.02	0.01	0.02	0.02	BDL	BDL	BDL	BDL	BDL
V	BDL	BDL	BDL	BDL	BDL	BDL	BDL	BDL	BDL

Zn	0.03	0.10	0.12	0.83	0.86	0.91	1.61	1.62	1.64
Sn	BDL	BDL	BDL	BDL	BDL	BDL	BDL	BDL	BDL
Mo	BDL	BDL	BDL	BDL	BDL	BDL	BDL	BDL	BDL
Sb	BDL	BDL	BDL	BDL	BDL	BDL	BDL	BDL	BDL
Ti	BDL	BDL	BDL	BDL	BDL	BDL	BDL	BDL	BDL
pH	7.26	7.77	7.87	3.15	3.18	3.33	2.67	2.63	2.66

Table A2: Complete sample results for 330-m seep and Lower Lion Creek. All concentrations are in mg/L.

	330-m Seep			**Lower Lion Creek**		
Species	**8-Jul**	**4-Aug**	**14-Aug**	**8-Jul**	**4-Aug**	**14-Aug**
F	4.97	8.41	5.24	0.89	1.21	BDL
Cl	4.12	2.95	21.63	BDL	BDL	20.72
NO2	1.19	BDL	BDL	BDL	BDL	BDL
Br	BDL	BDL	BDL	BDL	BDL	BDL
NO3	BDL	BDL	BDL	BDL	BDL	BDL
PO4	BDL	BDL	BDL	4.68	BDL	BDL
SO4	2527.6	2600.2	2314.7	195.04	297.92	411.19
O2	3.00	BDL	BDL	4.00	BDL	BDL
Al	57.43	52.97	50.83	9.30	11.76	13.17
As	BDL	BDL	BDL	0.03	BDL	BDL
B	0.63	0.60	0.46	0.47	0.14	0.39
Ba	BDL	0.05	0.06	BDL	0.05	0.07
Be	0.01	0.01	0.01	0.00	BDL	BDL
Ca	127.80	121.63	117.67	23.89	31.85	35.17
Cd	BDL	BDL	BDL	BDL	BDL	BDL
Co	0.34	0.32	0.31	0.07	0.10	0.11
Cr	BDL	BDL	0.00	BDL	BDL	BDL
Cu	2.20	2.06	1.91	0.26	0.32	0.34
Fe	167.11	145.33	136.16	9.41	12.84	14.39
K	3.90	1.20	0.73	0.57	0.97	1.05
Li	BDL	BDL	BDL	BDL	BDL	BDL
Mg2+	64.37	60.27	58.99	9.75	12.65	13.94
Mg+	64.53	61.66	58.98	9.68	12.44	13.78
Mn	31.09	29.70	27.92	5.65	8.29	9.32
Na	11.95	12.52	11.58	4.66	5.50	5.82

Ni	0.22	0.21	0.20	0.04	0.04	0.05
P	0.16	0.12	0.04	0.01	BDL	0.01
Pb	BDL	BDL	BDL	BDL	BDL	BDL
S	520.87	501.11	487.30	68.67	95.08	104.60
Se	BDL	BDL	BDL	BDL	BDL	BDL
Si	56.31	56.86	55.23	15.48	18.00	19.14
Sr	0.29	0.28	0.27	0.09	0.11	0.12
Tl	BDL	BDL	BDL	0.02	BDL	BDL
V	0.03	BDL	BDL	BDL	BDL	BDL
Zn	1.76	1.76	1.74	0.32	0.46	0.56
Sn	BDL	BDL	BDL	BDL	BDL	BDL
Mo	BDL	BDL	BDL	BDL	BDL	BDL
Sb	BDL	BDL	BDL	BDL	BDL	BDL
Ti	BDL	BDL	BDL	BDL	BDL	BDL
pH	2.61	2.59	2.59	3.61	3.35	3.28

Figure A3 shows the ratio of sulfate to total iron molar concentration in each of the water samples. The ratio is expected to be 2:15 at the AMD source for pyrite oxidation by ferric iron and 1:2 for pyrite oxidation by dissolved oxygen. Sulfate is much more persistent in the environment than iron, so the ratio is expected to be lowest in water that is most spatially or temporally removed from the AMD source. Since this ratio was calculated using total dissolved iron, we are assuming that any ferric iron in solution is the result of the oxidation of ferrous iron products of the pyrite oxidation reaction. It is notable that the 180-m seep has the highest sulfate to iron ratio, even higher than in Lion Creek. This differentiates the 180-m seep from the other acidic seeps. It is possible that this is because the 180-m seep has a different source of acidic water than the other seeps, or that the moss growing in the seep alters the chemical composition though microbially mediated processes.

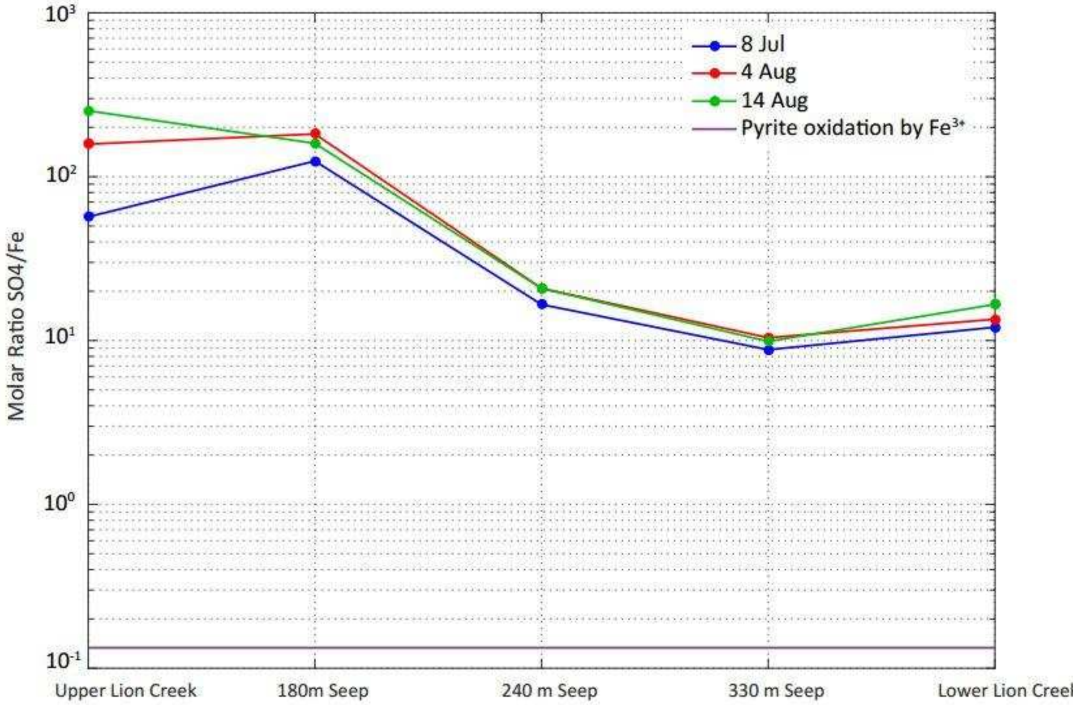

Figure A3: The sulfate to iron ratio at each of the five sampling sites on each of the sampling dates.

The relationship between σ_f and discharge was also investigated in this study (Figure 2.4). Here, it is explored further by distinguishing data points by their time of day (Figure A4) and proximity to precipitation events (Figure A5). There is a clear diel signal shown in Figure A4. Discharge increases at night when evapotranspiration stops and stream σ_f decreases, causing the scatter plot to shift right and downward at times when the sun is down.

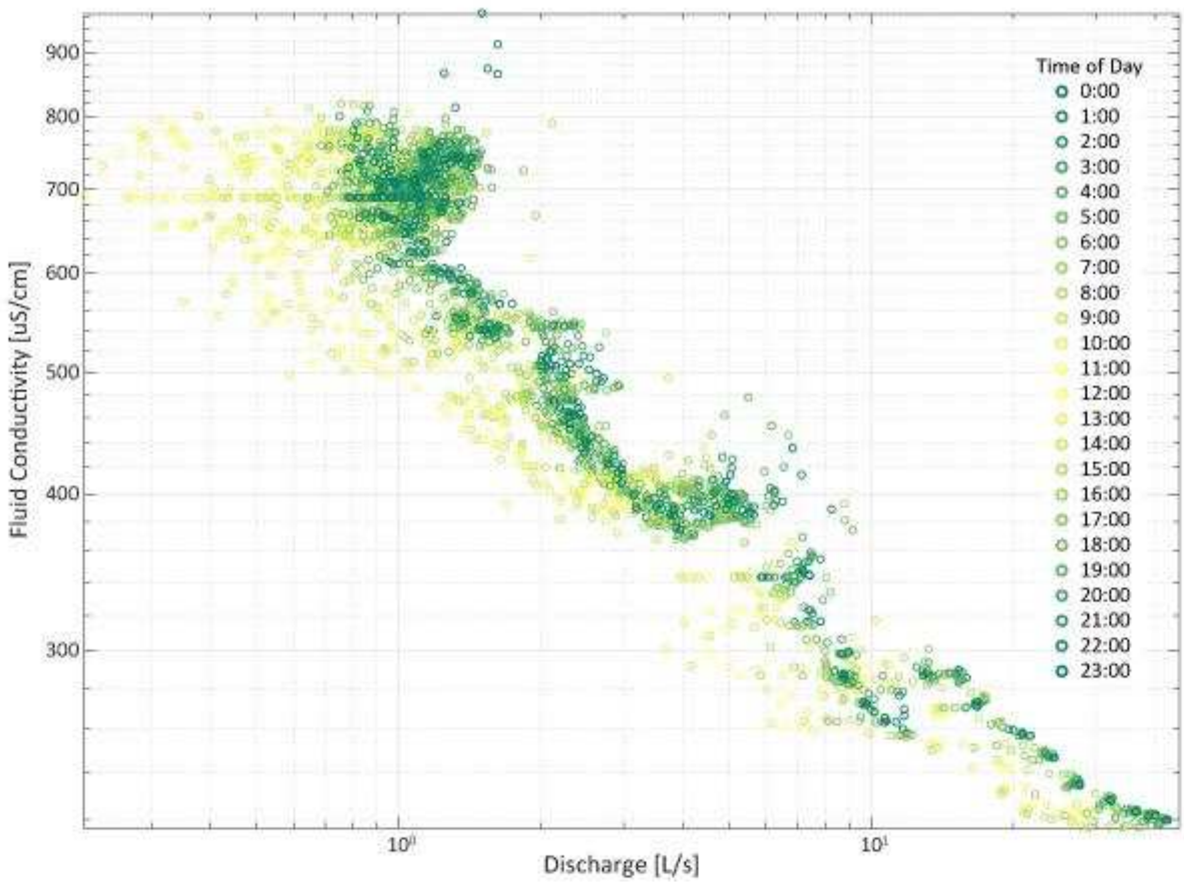

Figure A4: σ_f versus discharge plot color coded for time of day.

The plot was also color coded by the data point's proximity to a precipitation event. The scatter points represent the hourly average discharge and σ_f. Since the precipitation data is in daily totals, the data points were color coded turquoise if there was any rain during the day, pink if there was rain the previous day, and dark blue if there wasn't rain that day or the previous day. Figure A5 shows that many of the data points that are removed from the others are from days with precipitation or the day after precipitation. This is likely because precipitation slightly increases stream discharge as well as increases the steam σ_f, as shown in Figure 2.3b. This means that data points on days with precipitation should move up and to the right compared to data points on dry days.

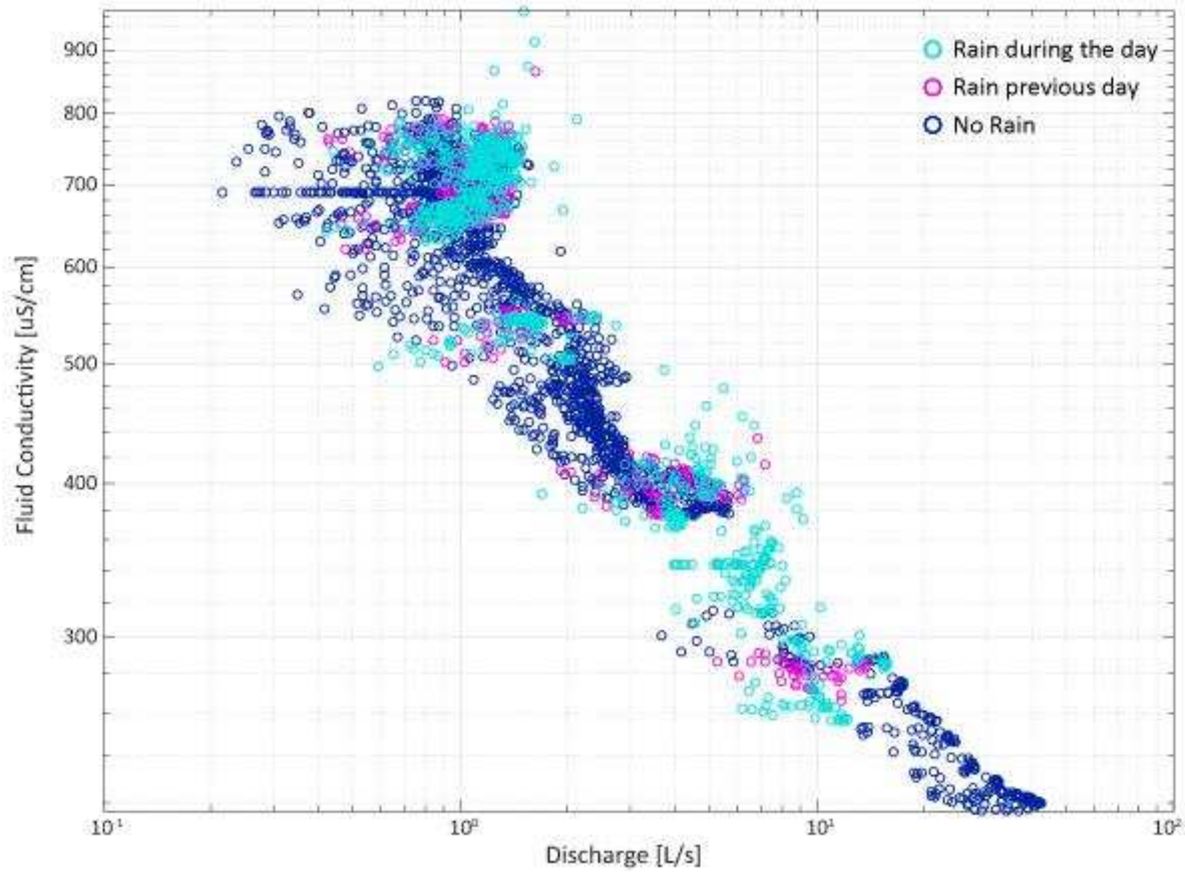

Figure A5: σ_f versus discharge plot color coded for the proximity to precipitation events.

TDS load was calculated using the stream discharge from the upper stilling well and the TDS calculated using the σ_f measured in Lower Lion Creek. The load, discharge, and σ_f are all plotted in Figure A6. The load has a notable diel variation, with higher loads at night when discharge is high and σ_f is slightly lower due to evapotranspiration.

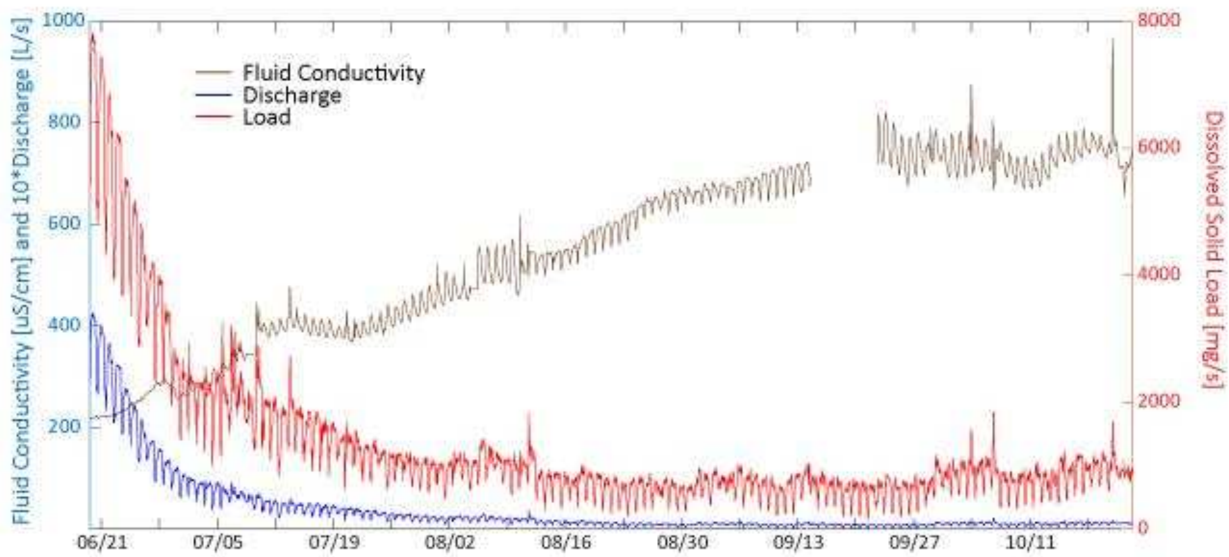

Figure A6: TDS load, discharge, and stream σ_f.

Further research at this field site should include water sampling at high enough resolution to recreate the load plot (Figure A6) and concentration-discharge plots (Figures A4 to A5) for individual AMD constituents rather than total dissolved solids. This will help interpret the seasonal dynamics of contaminants of concern.

APPENDIX B: TIME-LAPSE ERI

The replicate ERI surveys along Lion Creek are shown in Figures B1a-e, plotted as percent change in σ_b compared to the background 12 May 2015 survey. Table B1 shows the average apparent σ_b, range of apparent σ_b, stack deviation, alpha (tradeoff between data misfit and regularization in objective function) and final normalized RMS. The apparent σ_b values were used to explore the raw data; the range in apparent σ_b values generally decreased throughout the study period, and the increased contrast in σ_b values is apparent in the percent conductivity figures. The decrease in σ_b is expected over the field season since the seepage σ_f measured by the σ_f loggers decreases over the same time frame.

At 230 to 245 m, there is an area where the σ_b increases close to the ground surface over the field season. This area is just upstream of a large eroded area that contains a large seepage face. The seep σ_f decreases throughout the field season, but the σ_b increases in this area. This could be because over the course of the summer there is less fresh water in the shallow subsurface as the groundwater table recedes, allowing more acidic seepage water to infiltrate.

As the stream σ_f increases throughout the summer, the σ_b of the shallow subsurface shows increasing contrast. The σ_b of the upper and lower study reach increases by 10 to 15 percent compared to May 12th values, while σ_b from about 70 m to 180 m slightly decreases. The higher σ_b is likely the result of stream water of increasing σ_f entering the subsurface.   The contrast in σ_b suggests that stream water infiltrates in certain areas but not others.

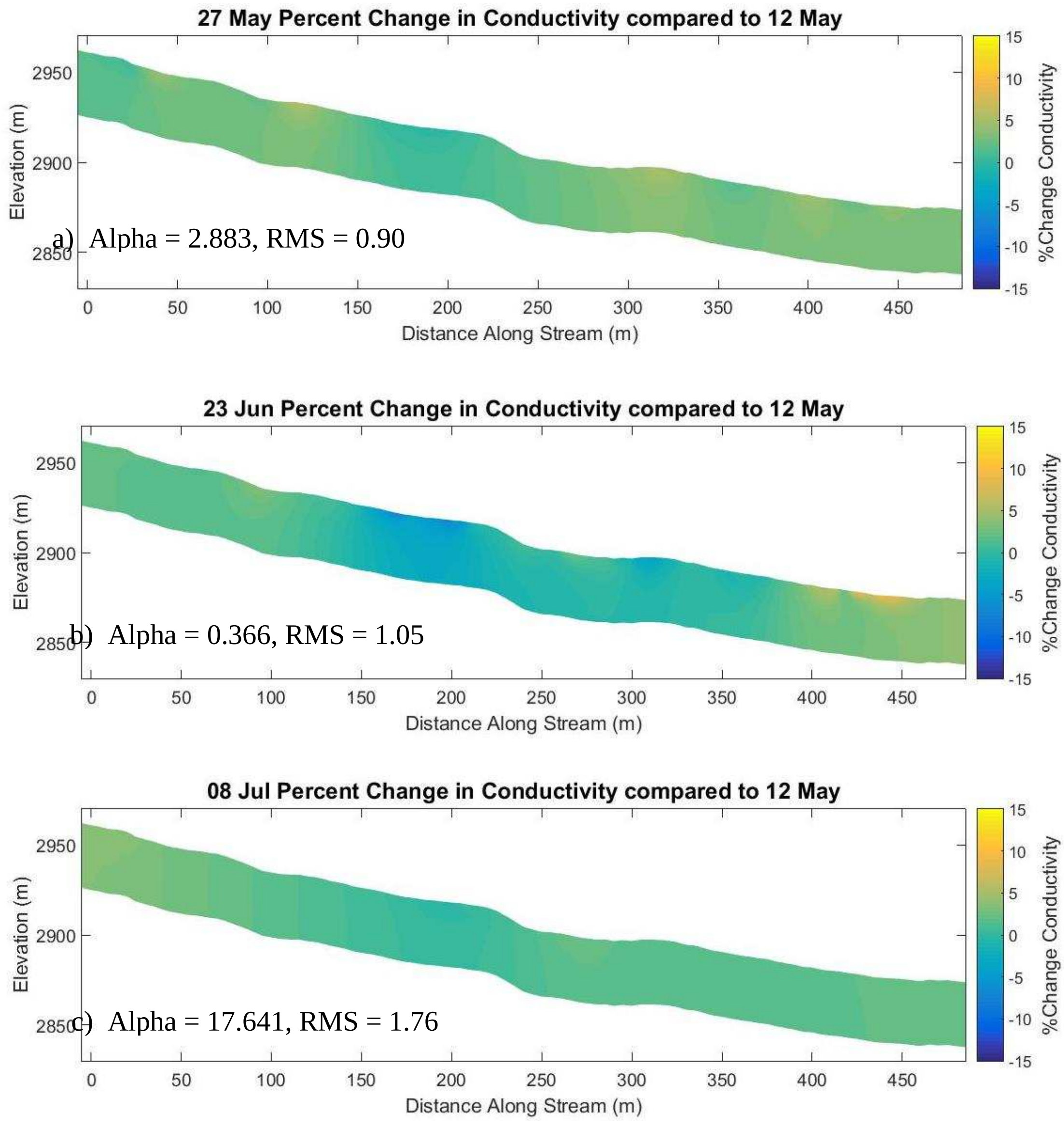
27 May Percent Change in Conductivity compared to 12 May
a) Alpha = 2.883, RMS = 0.90
Elevation (m)
Distance Along Stream (m)
%Change Conductivity
23 Jun Percent Change in Conductivity compared to 12 May
b) Alpha = 0.366, RMS = 1.05
Elevation (m)
Distance Along Stream (m)
%Change Conductivity
08 Jul Percent Change in Conductivity compared to 12 May
c) Alpha = 17.641, RMS = 1.76
Elevation (m)
Distance Along Stream (m)
%Change Conductivity

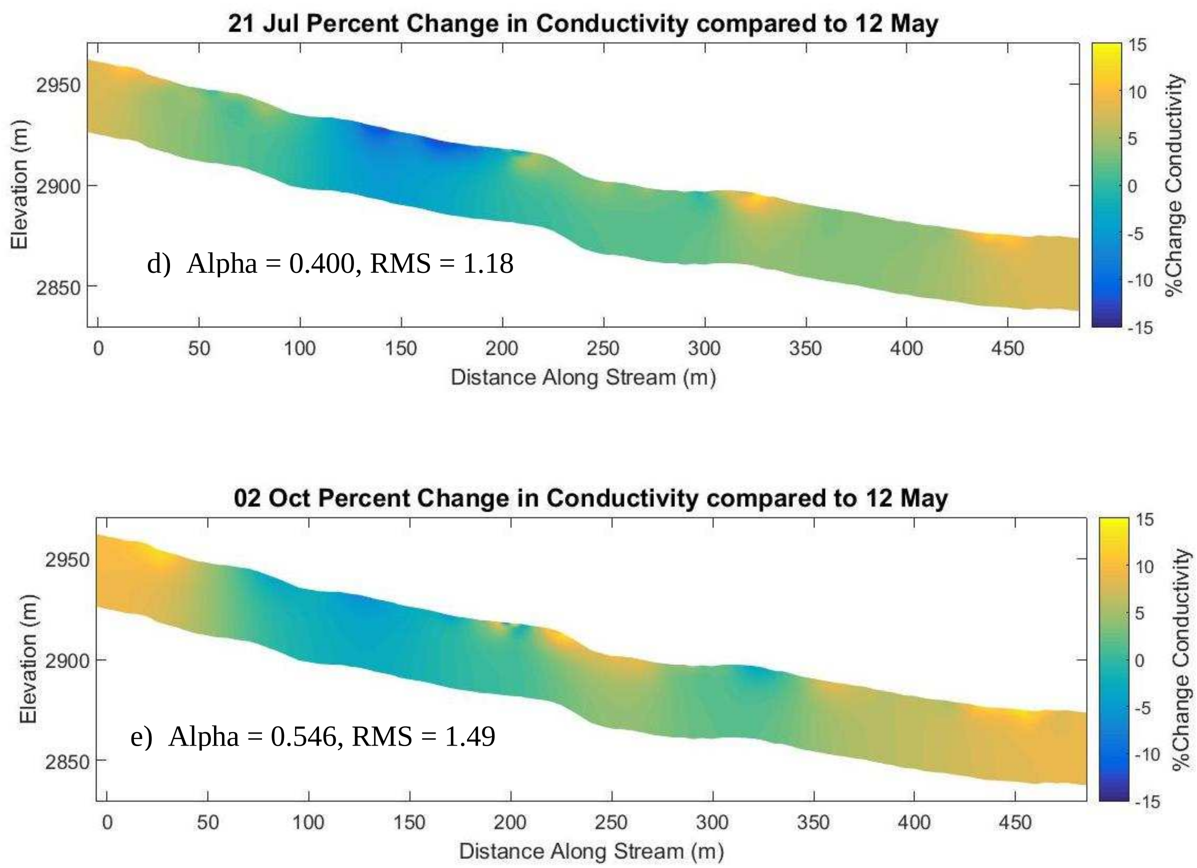

Figure B1: Figures B1a to B1e show the time lapse inversion results. The percent change in conductivity is calculated relative to the 12 May 2015 data set.

Table B1: The stack deviation and apparent σ_b statistics describe the time lapse ERI raw data sets. The alpha and RMS values describe the inversion results.

		12-May	27-May	23-Jun	8-Jul	21-Jul	2-Oct
Stack Deviation (%)	**Median**	0.18	0.18	0.14	0.17	0.20	0.21
	Mean	1.30	1.30	3.42	1.81	1.34	2.36
	Max	149.04	149.04	3312.02	413.22	185.32	593.74
	Std Dev	6.75	6.75	79.53	16.37	6.13	17.85
Apparent σ_b [mS/m]	**Median**	7.6	7.8	7.7	7.7	7.7	7.8
	Mean	7.7	7.8	7.4	7.9	8.0	7.6
	Std. Dev	3435.0	8.9	33.4	23.8	6.1	9.7
Alpha		0.001	2.883	0.366	17.641	0.400	0.546
RMS		1.40	0.90	1.05	1.76	1.18	1.49

APPENDIX C: TRACER TEST ERI RESULTS

In this appendix, we briefly present the ERI data that we collected during a hydrologic tracer test done by the USGS on 25 and 26 August, 2014. Two salts, NaBr and LiCl, were injected continuously into the stream starting at 19:30 on 25 Aug. Bromide is a conservative tracer at circumneutral pH, and lithium is conservative at low pH, so the recovery of the both species was compared. The salt solution was injected at 0 m in the study reach, corresponding to the location where the ERI transect parallel to the stream began and the upstream limit of our study reach. The location of tracer injection is shown in Figure C1. The goal of the tracer injection is to raise the concentration of the tracer elements above their background levels to a steady concentration in the stream, called a plateau concentration. Then, deviations from the plateau concentration down the study reach can be attributed to changing discharge. This test resulted in a detailed spatial profile of discharge in Lion Creek. Concurrent synoptic sampling yielded a spatial distribution of contaminant concentrations, and these two data sets can be used to find a metal loading profile along the study reach. This approach to mine site characterization is outlined in Kimball et al. (2002). The shape of the tracer breakthrough curve is indicative of transport parameters (Runkel 1998), and this along with detailed chemical data can be used to develop a reactive transport model which is valuable in the evaluation of remediation scenarios, as in Runkel and Kimball (2002).

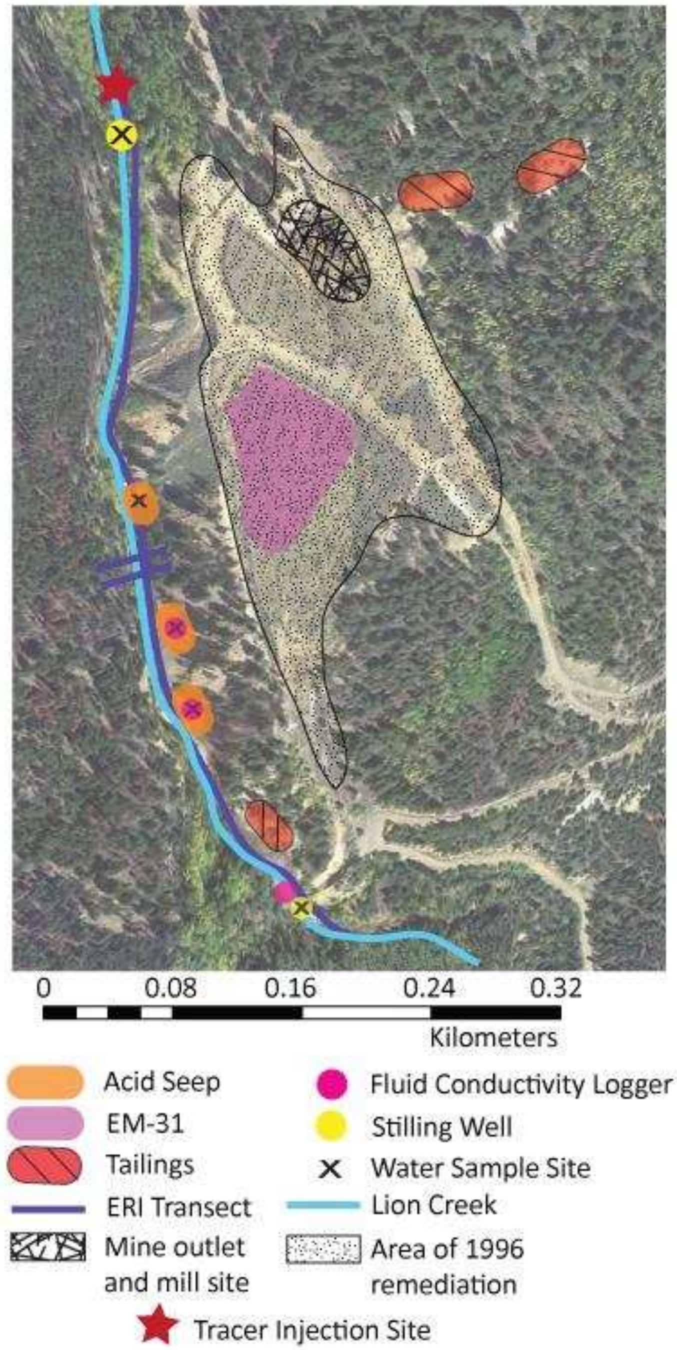

Figure C1: Overview of the study reach including the location of the tracer inject and the ERI transects used during the tracer injection.

During the USGS study, we collected ERI data in two transects perpendicular to the stream, shown in Figure C1. The transects cross the stream at 230 and 232 m along the study reach. Each transect consists of 24 electrodes spaced at 0.5 m intervals. A dipole-dipole survey of 231 quadripoles was collected over each transect ten times prior to the tracer injection and continuously during the injection. A finite element mesh was created with nodes paced at 0.25 m intervals in the x-direction and 0.5 m spacing in the z-direction, with larger spacing at the lateral and vertical edges of the mesh. One of the surveys prior to tracer injection was selected to be the reference σ_b model for each of the subsequent models, called the background. The inverted background survey was used as the starting point for each inversion of the subsequent datasets collected during the tracer test. The inversions were done as a time-lapse inversions, meaning the percent change from the background survey was computed. The surveys were collected as quickly as possible since the aim is to represent the distribution of the tracer at a snapshot in time, and long survey times can cause temporal smearing. To optimize speed, only two replicate measurements were collected at each quadripole, from which the coefficient of variation was calculated to be used as a data weight in the inversion scheme.

The goal of this was to define the hyporheic zone area, and to help inform the USGS's reactive transport modeling efforts. The difference between the background and the subsequent datasets is due to the high σ_f tracer entering the stream and mixing with water in the hyporheic zone, since that is likely the only process significantly changing σ_b over the course of two days. This allows us to separate the effects of the tracer from geologic features. The σ_b where the tracer penetrates is elevated, and this high σ_b area can be assumed to be the extent of the hyporheic zone. The background σ_b distribution and the percent σ_b difference between the background and plateau distributions are shown in Figure C2.

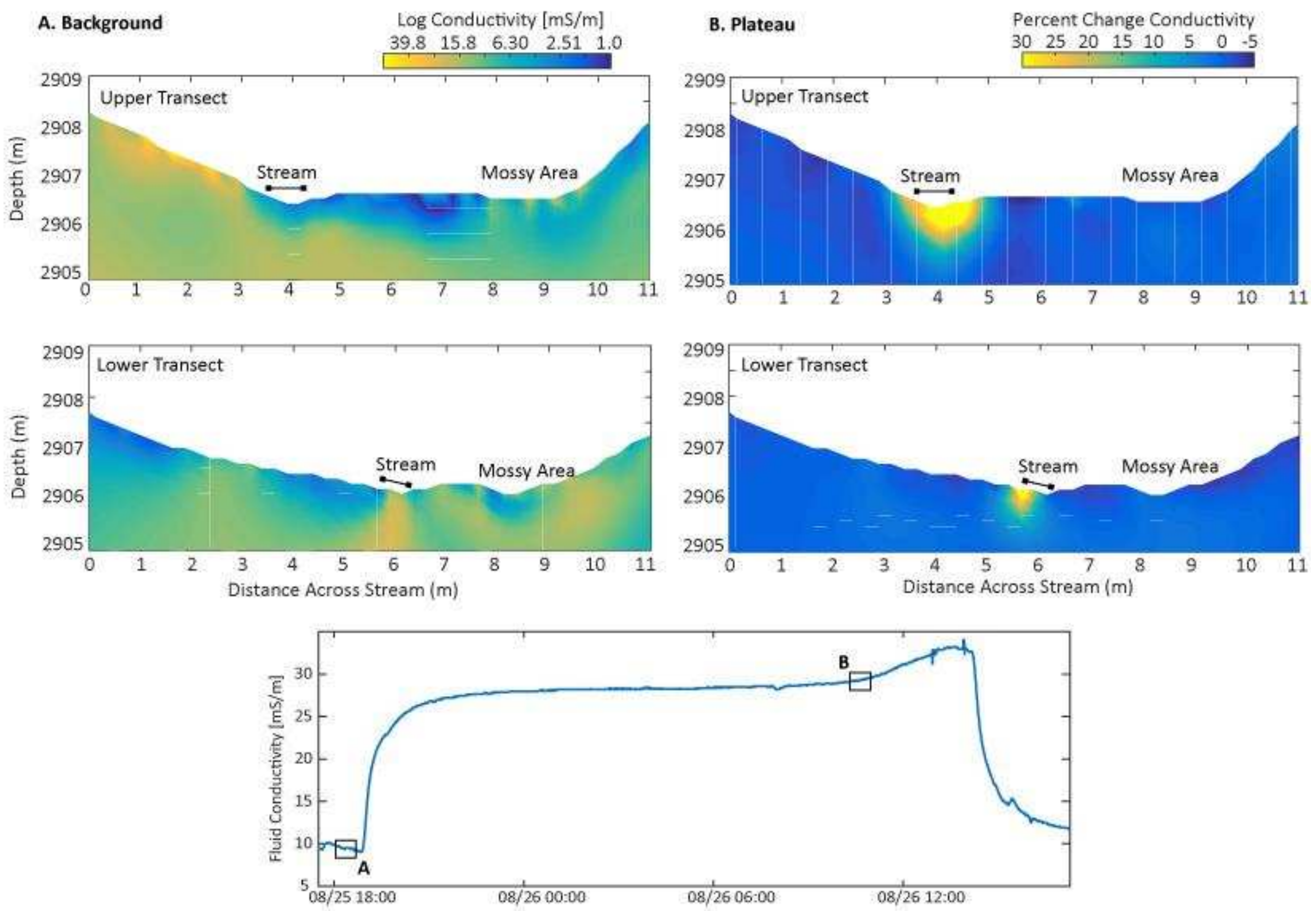

Figure C2: (a) The background log conductivity distribution is shown in the upper left, with the location of the stream and of a mossy area with some standing water during the tracer test annotated on the figures. (b) The percent change of the conductivity distribution between the tracer plateau and background conditions is shown on the right.

In Figure C2b, the yellow area represents the portion of the subsurface the tracer infiltrates. This area is commonly taken to be the extent of the hyporheic zone (Ward et al. 2010). Thus, from the percent change in conductivity image we can determine that the mossy area with standing water next to the stream does not interact with the stream since it was unaffected by the tracer. Knowing the extent of the hyporheic zone is important for determining what areas of the subsurface are in direct hydraulic connection with the stream. Though it could be instructive to repeat the tracer test in the vicinity of the tailings pile on the bank of Lion Creek to see how much of it is in contact with the stream, the tracer test was run in a less mine impacted section of the study reach because it is difficult to raise the stream σ_f far enough above its background in sections where the stream is already highly conductive.